Hydrogeochemistry and geothermometry of geothermal waters from the Pearl River Delta region, South China

Wei Zhengan [a, b], Shao Haibing [c], Tang Ling [d], Deng Bin [e], Li Hailong [f], Wang Chengshan [a, b, *]

[a] State Key Laboratory of Biogeology and Environmental Geology, China University of Geosciences (Beijing), Beijing, 100083, China

[b] School of Earth Sciences and Resources, China University of Geosciences (Beijing), Beijing, 100083, China

[c] Helmholtz Centre for Environmental Research-UFZ, Permoserstraße 15, 04318 Leipzig, Germany

[d] Team 935, Geology Bureau for Nonferrous Metals of Guangdong Province, Huizhou, 516001, China

[e] State Key Laboratory of Oil and Gas Reservoir Geology and Exploitation & College of Earth Science, Chengdu University of Technology, Chengdu, 610059, China

[f] Chinese Academy of Geological Sciences, Beijing, 100037, China

Abstract

This study focuses on the hydrogeochemical features and reservoir temperatures of the geothermal waters in the Pearl River Delta (PRD) region of south China, which can provide useful information and overall assessments on the geothermal potential and 24 geothermal well waters and 8 hot spring waters were collected from the inland and coastal areas of the PRD region. Hydrochemical and isotopic analysis ($\delta^{18}O$, $\delta^{2}H$, ^{3}H), empirical chemical geothermometer, mineral saturation state, and silica-enthalpy mixing model have been applied in the PRD thermal waters. The hydrochemical facies of inland geothermal waters are of the bicarbonate-dominated and sulfate-dominated type, and the coastal waters are of chloride-dominated type. Chemical compositions of the geothermal waters reveal strong fluid-rock interactions, the common ion effect, mixture between seawater and thermal waters in coastal waters, and mixing process between cold groundwater and thermal waters in inland waters. Hydrochemical results and enriched heavy isotopes suggest that coastal waters are recharged by local precipitation and seawater. $\delta^{18}O$ and $\delta^{2}H$ compositions of the inland waters plot along the Local Meteoric Water Line (LMWL), indicating the recharge of local precipitation.

The activities of tritium verify that inland and coastal waters have modern meteoric components. Reservoir temperatures are mainly influenced by the degassing of CO_2 and cold groundwater/seawater mixing. Calculations of chalcedony geothermometers, mineral saturation states, and silica-enthalpy models provide the most reliable estimations of reservoir temperature: 90-154 ℃ for inland thermal waters, 104-156 ℃ for coastal thermal waters, likely indicating low-mid temperature geothermal resources in the PRD region.

Keywords

Geothermal waters; Hydrogeochemistry; Geothermometers; Isotopes; Pearl River Delta region; South China

1. Introduction

Since the late 1970s the implementation of the Reform and Open Policy proposed by the Chinese government has transformed the Pearl River Delta (PRD) region from a fisheries and agricultural economy to one of the major manufacturing hubs in the world (Lu et al., 2016). The rapid development of urbanization and economic growth have the standard of living rocketed upward, making the PRD the richest district in China, but in the meantime the looming shortage of energy, environmental deterioration, global warming crisis, and high levels of carbon emissions have been increasingly accentuated in the past decade. Given the concerns over climate and environment change brought by fossil fuel combustion, geoscientists are focusing more on renewable energy and clean and sustainable natural resources, e.g., geothermal energy resources.

Conventional geothermal energy in the world is extracted where hot rock and groundwater have come together naturally, which provide a ready supply of superheated water or steam (Kerr, 1991). More advanced geothermal resources, including geopressured geothermal systems, hot dry rocks and magma, have been gradually discovered and developed since the early 1970s (Huang and Liu, 2010; Kerr, 1982; Mock, 1992). It's reported that dozens of countries started to utilize geothermal energy over 2000 years ago (Fournier and Potter, 1982). The development and utilization of geothermal energy has become especially rapid in the last 50 years (Lund and Boyd, 2016; Lund and Freeston, 2001; Stefansson, 2000). The utilization of geothermal resources, to a great extent, depends on the hot water or steam temperature. Low temperature (25–90 ℃) geothermal resources are mainly used for direct utilization such as heating, cooling, fish farming and other agricultural purposes (Luo et al., 2015; Noorollahi et al., 2017). The moderate temperature (90−150 ℃) geothermal resources are generally applied for direct use and electricity generation (Pandey et al., 2018). High temperature (>150 ℃) geothermal resources are mostly useful for power electricity.

Geothermal resources are widely distributed across China and the direct utilization of geothermal resources for medical treatment, bathing, and cooking has lasted for thousands of years. The largest application of geothermal resources nowadays is for heating/cooling, spa treatment and greenhouse cultivation (Lund and Boyd, 2016). According to statistics from previous studies, over 4000 hot waters (geothermal waters, mine waters, and springs) with temperatures above 25 ℃ have been discovered, in particular, more than 300 hot springs in Guangdong province, third only to Tibet and

Yunnan province in China (Liao, 2012; Wang et al., 2018; Zhao and Wan, 2014). Furthermore, more and more low-moderate temperature geothermal resources continue to be found in the PRD region. Numerous geothermal waters have been used for bathing and medicinal purposes for many years and plenty of the geothermal areas in the PRD region have been transformed into distinguished tourist resorts especially for those hot springs located in Jiangmen, Guangzhou, and Huizhou city within the region. The Chinese government and local authorities have implemented a series of exploratory investigations and energy policies in last five years, which can lead to further utilization and study of the geothermal resources in this region.

More attention has been given to geothermal waters or fluids in different geothermal systems all over the world, and detailed investigations have focused on: (1) the hydrogeochemical processes reflected by water–rocks interactions (Guo, 2012; Park et al., 2006; Pastorellia et al., 1999; Verma et al., 2006); (2) the origin of geothermal fluids by using stable isotope ratios (Chenaker et al., 2018; Pasvanoglu and Celik, 2018; Portugal et al., 2005; Yurteri and Simsek, 2017); (3) the reservoir temperature based on minerals saturation states and chemical geothermometers (Mohammadi et al., 2010; Pirlo, 2004; Rezaei et al., 2019; Tian et al., 2018). Geothermal waters from Guangdong province appear to be no exception. In recent years, many researchers have examined in detail the chemical and isotopic composition of geothermal fluids, which has revealed the origins, reservoir temperatures and hydrogeochemistry of geothermal fluids through the application of isotopic data, geothermometers and fluid-mineral equilibria on the thermal waters in Guangdong. Almost all studies have highlighted geothermal areas outside the PRD region, such as Yangshan (Yin et al., 2017), Yangdong (Wang et al., 2018), Xinzhou (Lu et al., 2017), Fengshun and Xinyi geothermal fields (Li et al., 2018) , but only a few have considered geothermal areas or systems to draw the hydrogeochemical features of geothermal fluids from the PRD region, i.e. Dongguan (Mao et al., 2015) and Jiangmen (Chen et al., 2016; Wang et al., 2018). And no comprehensive research to determine the hydrogeochemical properties and reservoir temperatures of the region has been carried out.

By using new hydrochemical and isotopic data from thirty-two geothermal waters of the PRD region, this study is aimed to examine the hydrogeochemistry and geothermometry of geothermal waters from the PRD region to provide information on the geothermal potential and an overall assessment of: (i) describing the hydrogeochemical characteristics, (ii) determining the origin of geothermal waters, (iii)

estimating the reservoir temperatures. To verify the aims, a combination of hydro-geochemistry (including isotope and geochemistry), various empirical geothermometers, modeling of mineral saturation states, and silica-enthalpy mixing model are applied to understanding the functioning of the geothermal system.

2. Study area

2.1 Geography and climate

The Pearl River Delta (PRD) region is located in the central Guangdong province, bordered by the South China Sea to the south and by the inland areas to the west, north and east (see Fig. 1). The terrain is generally high in the north and low in the south, incorporating plains, hills, mountains, and plateaus (Pei et al., 2018).The climate in the region is highly controlled by the sub-tropical East Asian monsoon. It results in hot and humid summers with heavy rains, followed by warm and dry winters with little frost and snow but very often heavy fogs. The average annual temperature is 21.8 °C and the average precipitation is 1789.3 mm, accompanied by an average evaporation up to 1100 mm per year (Pei et al., 2018). Surface runoffs in the form of streams and rivers widely exist in the region. However, they are susceptible to flooding and drought events due to concentrated rainfalls brought by the typhoons.

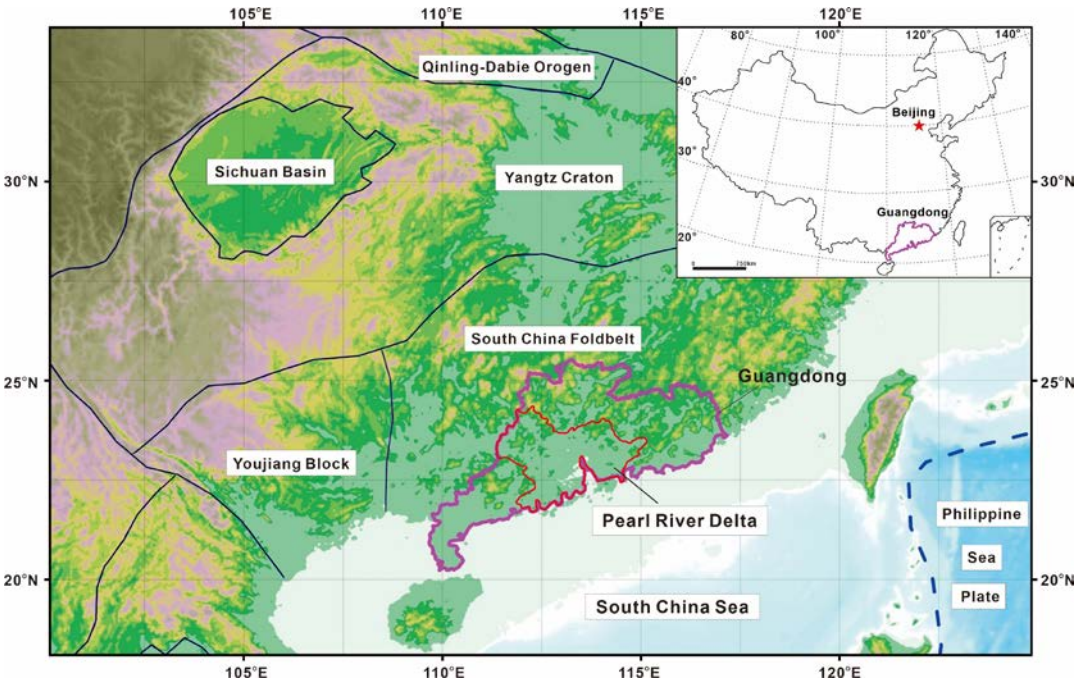

Fig. 1 Tectonic location of the Pearl River Delta region and topographic map of South China.

2.2 Geological and hydrological setting

Pearl River Delta (PRD), a large basin in southeastern China, is characterized by the confluence of various rivers and located in South China Fold belt of the east Eurasian plate. The PRD is bounded in the north by the Yangtze Craton and in the west by the Youjiang Block (Fig 1). This region consists of sets of tight linear folds, which form two anticlinorium belts extending over 600 km in a NEE direction and play an important influence on stratigraphic distribution and regional magmatism (GBGMI, 1988). Tectonic evolution can be concisely described as follows: (1) geosyncline phase from Sinian to Silurian; (2) platform phase from Devonian to Middle Triassic; (3) active continental margin stage from Late Triassic to Quaternary (GBGMI, 1988; Huang and Chu, 1995). Stratigraphic sequence can be summarized from bottom to top as follows: (1) a metamorphosed Pre-Cambrian basement overlain by a discontinuous Paleozoic to Mesozoic terrigenous sequence with carbonate units; (2) Upper Mesozoic to Tertiary volcanism and intrusions break up the sedimentary bedrock; (3) Quaternary marine to continental facies fill the depressions in the Pearl River Delta region (Lancia et al., 2020).

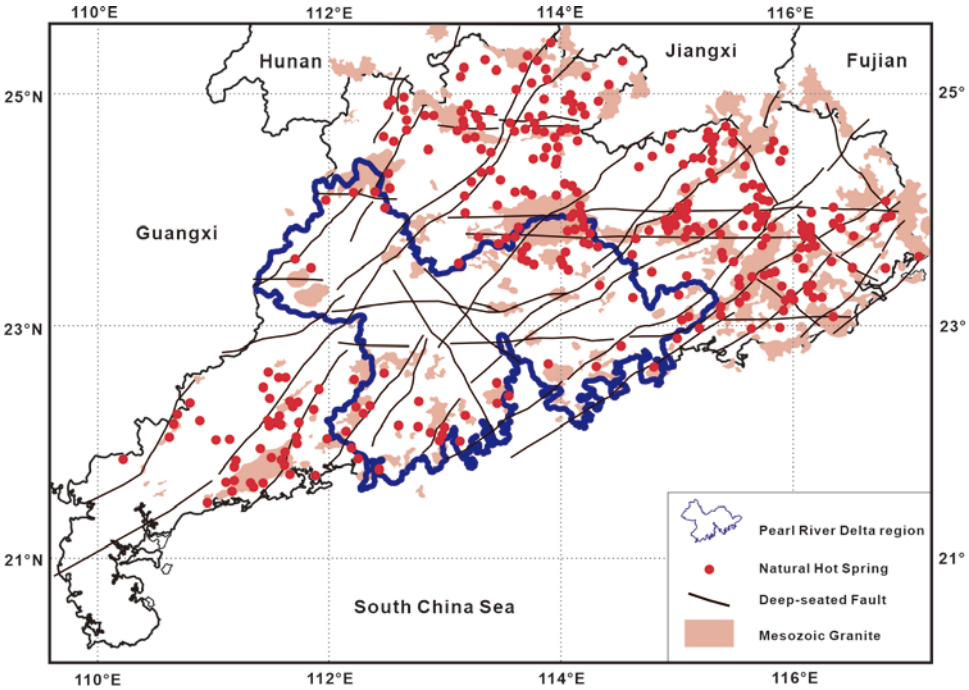

Fig. 2 Geological sketch map of Guangdong, showing the distribution of hot springs and Mesozoic exposed granites and the extending of major faults (Xi et al., 2018).

The extensive crust–mantle interaction in geological history can be reflected by the multistage intrusions (Zhou and Li, 2000; Zhu et al., 2010). Exposed intrusive rocks (Fig. 2) occupy an area of more than 30% of Guangdong with the occurrence of batholith and stock (Xi et al., 2018), among which Mesozoic granites are the most

extensive igneous rocks, followed by the monzonitic granites and granodiorites (Lin et al., 2006). Tertiary strike-slip faults and recent normal faulting can be recognizable in the NE−SW, E−W and NW−SE direction (Fig. 2). The major lineaments, such as Guangzhou fault and Shenzhen fault, are of in the trend of NE−SW. Secondary faults intersect the NE-SW main tectonic systems (Lancia et al., 2020). Bouguer gravity data indicate that the Guangzhou deep fault throughout the Pearl River Delta region reaches as much as 30 km in depth (Ren et al., 2011).As can be seen in Fig. 2, most hot springs are located along the NE−SW faults and near the junctions of faults. They can often be found around the granites, which shows that the occurrence of hot spring is a particular phenomenon associated with the lithostratigraphic features and structural conditions. The circulation of thermal water is closely related to fracture zones. Simultaneously, repeated activities of deep–seated faults provide favorable conduits for groundwater migration (Chen et al., 2016).

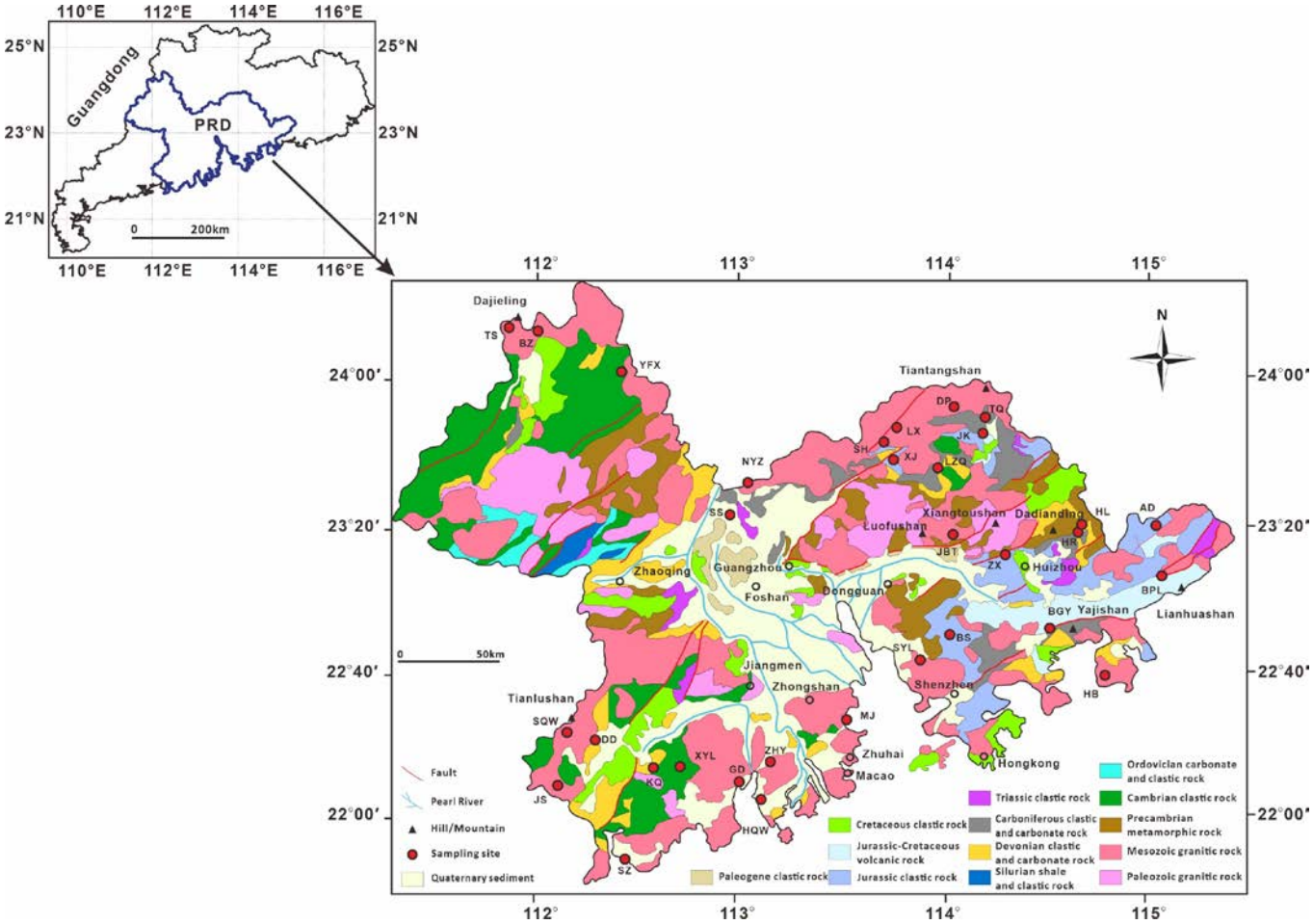

Fig. 3 Geological map of the Pearl River Delta region, showing the sampling sites.

According to different types of lithology and the porosity of the rock in the study

area, four hydro–stratigraphic groups can be recognized (Fig. 3). Quaternary sediments cover large parts of the delta plain close to the coastal line. The old terrestrial sediments (sands and gravels) were overlain by marine silt and clay. Then a younger terrestrial unit (sands and gravels) was deposited above these marine sediments, and afterwards a layer of younger marine sediment comprised of silt and clay was deposited at the top (Zong et al., 2009). Red sandstones, siltstones and conglomerates in Jurassic to Tertiary are lack of ground water, due to their low permeability and lack of fissures. Devonian to Carboniferous carbonate rocks, with well-developed fracture–karst systems in them, can be identified as the most important reservoirs in this area. Granites and metamorphic rocks with compact structure and low permeability are assumed to be lack of ground water except for fractured metamorphic rocks and intrusions rich in fissure water (Zhang, 2009).

3. Methodology and materials

In order to investigate the hydrothermal and geochemical feature of the PRD area, a field sampling campaign was conducted from March to May 2019. During the campaign, a total of 32 thermal water samples were collected from 32 locations. Among them, twenty–four of these samples were taken from geothermal wells, and eight water samples came from natural hot springs. The information about the sample types, locations, and sampling dates are presented in Table 1. For each sampling site, three different types of samples were collected: (1) a 500 ml liquid sample (acidified and filtered) for cations analysis; (2) a 500 ml sample, passed through a 0.45 μm filter to remove sediment particles, for major anions and dissolved silica measurements; and (3) a 500 ml sample for stable isotope analysis. All these thermal water samples were not diluted and cooled on site because the temperatures of these samples did not reach the boiling point. It should be pointed out that water samples for the determination of dissolved SiO_2 were not diluted with deionized waters according to the ratio of 1：10, which probably caused SiO_2 precipitation in the geothermal waters. However, the concentrations of dissolved SiO_2 were calculated based on the contents of dissolved H_2SiO_3 in this study and the computations show that 75% of the thermal waters have SiO_2 concentrations lower than 100mg/L (Table 2). And therefore, we believe that water samples that were not diluted also are effective and that these calculations also are valid. Before collecting the sample, high-density polyethylene (HDPE) bottles were rinsed twice with deionized water. Every bottle was sealed with paraffin before it was

transported to the laboratory. Physicochemical parameters of these thermal water samples including oxidation–reduction potential (ORP), electrical conductivity (EC), pH and total dissolved solids (TDS) were measured on site by using Water Quality Multiparameter Probes (AZ–86031), which was calibrated prior to sampling. Water temperature was determined by Infrared Thermometer and the measurement error is estimated to be within ± 0.2 °C. The coordinates of each sampling location were recorded by a hand GPS and also marked on a geological map.

Table 1 Sampling locations and dates

No	Sample ID	Location	Coordinates		Sampling date	Type	Category
			N	E			
1	HR	Hengli, Huizhou	23°15'57.020"	114°38'43.361"	27.03.2019	thermal well	Inland
2	ZX	Huicheng, Huizhou	23°12'08.896"	114°21'32.731"	02.04.2019	thermal well	Inland
3	BPL	Baipengzhu, Huizhou	23°03'35.374"	115°03'09.155"	04.04.2019	thermal well	Inland
4	HL	Hengli, Huizhou	23°16'38.73"	114°38'27.89"	06.04.2019	thermal well	Inland
5	LZQ	Yonghan, Huizhou	23°34'03.526"	113°59'36.265"	07.04.2019	thermal well	Inland
6	LX	Liangkou, Guangzhou	23°41'30.667"	113°42'06.534"	08.04.2019	thermal well	Inland
7	SH	Wenquan, Guangzhou	23°39'03.319"	113°38'55.349"	09.04.2019	thermal well	Inland
8	NYZ	Qingcheng, Qingyuan	23°33'04.633"	113°07'20.471"	10.04.2019	thermal well	Inland
9	SQW	Datian, Jiangmen	22°20'08.876"	112°13'18.768"	16.04.2019	thermal well	Inland
10	JS	Naji, Jiangmen	22°07'16.896"	112°10'13.044"	19.04.2019	hot spring	Inland
11	AD	Andun, Huizhou	23°15'57.193"	115°01'54.491"	29.04.2019	thermal well	Inland
12	JBT	Boluo, Huizhou	23°16'34.219"	114°04'28.805"	06.04.2019	thermal well	Inland
13	TS	Lanzhong, Zhaoqing	24°11'57.242"	111°54'56.437"	15.04.2019	thermal well	Inland
14	DP	Dipai, Huizhou	23°50'44.326"	114°04'15.222"	08.04.2019	thermal well	Inland
15	SYL	Gaungming, Shenzhen	22°42'53.644"	113°53'16.098"	02.05.2019	hot spring	Inland
16	DD	Liangxi, Jiangmen	22°17'33.954"	112°18'07.639"	18.04.2019	thermal well	Inland
17	BS	Tangxia, Dongguan	22°48'44.960"	114°03'31.903"	28.04.2019	thermal well	Inland
18	SS	Lubao, Foshan	23°22'06.283"	112°58'06.996"	11.04.2019	thermal well	Inland
19	XJ	Paitan, Guangzhou	23°33'59.468"	113°46'22.883"	10.04.2019	thermal well	Inland
20	BGY	Huiyang, Huizhou	22°50'37.378"	114°31'47.791"	03.04.2019	thermal well	Inland
21	YFX	Fenggang, Zhaoqing	24°00'21.089"	112°28'37.974"	13.04.2019	hot spring	Inland
22	BZ	Zhongzhou, Zhaoqing	24°09'34.942"	112°11'00.485"	12.04.2019	hot spring	Inland
23	TQ	Longtian, Huizhou	23°49'22.368"	114°14'04.308"	07.04.2019	hot spring	Inland
24	JK	Longtian, Huizhou	23°45'43.402"	114°13'33.071"	30.04.2019	thermal well	Inland
25	KQ	Baisha, Jiangmen	22°09'21.254"	112°36'25.045"	18.04.2019	hot spring	Coastal
26	XYL	Sanhe, Jiangmen	22°11'31.369"	112°44'44.711"	17.04.2019	thermal well	Coastal
27	GD	Yamen, Jiangmen	21°47'54.409"	112°28'48.529"	23.04.2019	thermal well	Coastal
28	HB	Pinghai, Huizhou	22°39'27.54"	114°47'59.72"	01.04.2019	thermal well	Coastal
29	SZ	Wencun, Jiangmen	21°47'54.496"	112°28'48.425"	22.04.2019	hot spring	Coastal
30	MJ	Nanlang, Zhongshan	22°25'14.120"	113°33'52.938"	26.04.2019	hot spring	Coastal
31	HQW	Pingsha, Zhuhai	22°03'29.196"	113°07'57.504"	25.04.2019	thermal well	Coastal
32	ZHY	Doumen, Zhuhai	22°15'00.018"	113°11'22.297"	24.04.2019	thermal well	Coastal

Concentrations of cation, anion, and dissolved silica and isotopic compositions ($\delta^{18}O$, $\delta^{2}H$, and ^{3}H) analysis were carried out at the laboratory of Institute of

Hydrogeology and Environmental Geology, Chinese Academy of Geological Sciences. Concentrations of bicarbonate (HCO_3^-), fluoride (F^-), chloride (Cl^-), sulfate (SO_4^{2-}), nitrate (NO_3^-), carbonate (CO_3^{2-}), lithium (Li^+), strontium (Sr^{2+}), sodium (Na^+), potassium (K^+), magnesium (Mg^{2+}), calcium (Ca^{2+}) and dissolved silica (SiO_2) were analyzed by using ICP–AES (ICAP6300, Thermo Fisher Scientific), which has the limit of detection of 0.02mg/L. Stable Isotopic ($\delta^{18}O$ and δ^2H) investigation was analyzed using Wavelength Scanning Cavity Ring–Down Spectroscopy (L2130i) with the uncertainties of less than 0.2‰. The tritium (^3H) contents were measured using Liquid Scintillation Spectrometer (Quantulus1220), and the determination of tritium isotopes follows the precision of less than ± 0.6 TU. Charge-balance error (CBE) of these geothermal waters is less than 5 %, which is within the limits of acceptability. Detection results of main cations, anions and isotopes are presented in Table 2. Water isotope ($\delta^{18}O$ and δ^2H) analyses were reported in ‰ relative to the Vienna Standard Mean Ocean Water (VSMOW) standard.

Table 2 Hydrochemical and isotopic compositions of thermal waters in the study area

Sample ID	T	pH	EC	TDS	Na^+	K^+	Ca^{2+}	Mg^{2+}	SO_4^{2-}	HCO_3	CO_3^{2-}	Cl^-	F^-	SiO_2	Li^+	Sr^{2+}	δ^2H	$\delta^{18}O$	^3H	CBE	Water type
HR	93.0	7.74	2618	1336	314.50	18.00	12.81	0.27	108.70	634.60	0.00	57.77	14.02	171.23	1.52	0.34	-44	-6.7	0.5±0.5	-0.40	Na-HCO3
ZX	58.1	7.99	1102	575	121.10	6.02	11.10	0.06	36.56	262.40	0.00	17.52	13.00	105.62	0.29	0.32	-44	-7.0	0.7±0.5	-0.41	Na-HCO3
BPL	52.9	7.95	841	426	86.70	3.28	11.40	0.01	32.40	198.30	0.00	11.20	11.67	70.70	0.18	0.31	-48	-7.5	0.8±0.5	-0.43	Na-HCO3
HL	93.2	8.50	2486	1280	303.00	18.24	12.01	0.21	107.60	573.60	18.00	57.77	13.84	173.23	1.55	0.29	-43	-6.6	0.5±0.5	-0.39	Na-HCO3
LZQ	65.8	7.86	1034	546	99.46	5.45	20.93	0.23	20.99	288.60	0.00	11.55	8.91	88.85	0.35	0.34	-42	-6.8	0.7±0.6	-0.45	Na-HCO3
LX	51.2	7.82	601	311	55.94	2.21	8.70	0.01	11.60	146.40	0.00	8.75	8.44	67.54	0.10	0.19	-43	-6.9	1.0±0.6	-0.45	Na-HCO3
SH	57.1	7.99	772	393	63.70	2.25	13.62	0.01	9.83	201.40	0.00	7.00	9.73	85.46	0.18	0.21	-43	-6.9	0.4±0.4	-0.48	Na-HCO3
NYZ	61.2	8.77	584	304	68.21	3.00	6.57	0.01	24.80	103.70	12.00	22.76	8.33	52.46	0.26	0.19	-38	-6.2	0.9±0.6	-0.38	Na-HCO3
SQW	54.5	8.61	506	259	48.44	2.06	8.37	0.01	6.02	106.80	9.00	5.25	0.13	64.32	0.16	0.09	-44	-7.0	0.6±0.6	-0.37	Na-HCO3
JS	67.1	8.94	722	379	88.30	2.19	3.56	0.01	32.50	122.00	18.00	12.95	13.08	84.62	0.29	0.07	-41	-6.5	0.5±0.5	-0.36	Na-HCO3
AD	60.1	8.51	728	367	79.15	2.59	10.14	1.13	32.83	140.30	6.00	12.25	13.78	66.18	0.20	0.47	-45	-7.2	1.1±0.6	-0.38	Na-HCO3
JBT	38.6	7.80	558	288	41.40	3.43	18.08	0.20	12.67	146.40	0.00	5.95	2.50	55.82	0.12	0.28	-42	-6.7	1.2±0.5	-0.45	Na-Ca-HCO3
TS	78.0	8.60	450	235	23.82	2.32	11.48	0.28	4.46	80.54	6.00	2.45	2.38	79.62	0.06	0.06	-42	-6.9	1.1±0.5	-0.44	Na-Ca-HCO3
DP	37.0	7.61	596	305	43.20	3.11	31.10	0.41	27.59	134.20	0.00	6.30	5.08	52.10	0.09	0.31	-42	-6.7	0.9±0.6	-0.38	Na-Ca-HCO3
SYL	59.8	8.03	1288	682	168.80	6.82	22.97	0.09	141.00	183.10	0.00	78.08	10.59	68.64	0.60	0.51	-44	-6.9	0.7±0.5	-0.35	Na-HCO3-SO4-Cl
DD	67.2	9.04	542	281	62.35	2.73	2.66	0.01	7.68	91.53	24.00	5.25	8.37	75.72	0.17	0.05	-45	-7.1	0.5±0.5	-0.34	Na-HCO3-CO3
BS	36.5	8.42	739	323	33.48	2.55	37.54	6.21	7.87	198.30	6.00	5.95	3.87	19.03	0.06	1.57	-46	-7.1	1.3±0.6	-0.47	Ca-Na-HCO3
SS	41.9	7.38	1493	756	8.88	3.88	154.20	13.78	13.55	530.90	0.00	10.15	0.55	19.15	0.04	0.64	-39	-6.3	0.6±0.6	-0.51	Ca-HCO3
XJ	60.9	7.85	634	341	29.84	3.60	39.26	1.08	36.60	152.50	0.00	5.25	5.05	67.44	0.06	0.57	-41	-6.7	1.2±0.6	-0.46	Ca-Na-HCO3-SO4
BGY	42.9	7.93	606	316	6.26	1.83	64.34	5.68	87.63	122.00	0.00	3.50	0.80	24.34	0.00	1.42	-43	-6.5	1.2±0.5	-0.46	Ca-HCO3-SO4
YFX	65.9	9.33	408	216	39.08	1.86	4.38	0.01	12.69	43.93	24.00	4.55	4.34	98.62	0.07	0.04	-46	-7.5	0.5±0.5	-0.33	Na-CO3-HCO3
BZ	42.4	9.33	601	311	68.35	2.64	3.71	0.01	30.49	48.81	30.01	12.25	12.60	100.77	0.28	0.03	-43	-7.1	0.7±0.6	-0.28	Na-CO3-HCO3
TQ	58.6	7.71	1782	926	76.02	5.97	163.60	4.40	494.80	85.42	0.00	5.25	2.97	86.46	0.14	3.66	-42	-6.8	0.7±0.4	-0.40	Ca-Na-SO4
JK	58.9	7.90	1586	783	127.30	8.03	65.20	2.63	243.20	201.40	0.00	15.76	6.26	112.77	0.46	1.58	-42	-6.8	0.5±0.5	-0.39	Na-Ca-SO4-HCO3

KQ	86.9	8.00	2084	1077	284.20	12.56	14.82	0.07	67.36	332.50	0.00	232.80	11.19	118.23	1.26	0.42	-42	-6.9	0.5±0.5	-0.41	Na-Cl-HCO3
XYL	67.6	7.65	1838	934	262.80	7.64	36.71	0.72	38.28	109.80	0.00	402.70	7.20	66.38	1.09	1.01	-43	-6.8	0.5±0.5	-0.35	Na-Cl
GD	63.0	8.58	1014	520	132.00	3.99	10.92	0.01	8.83	79.50	9.00	169.79	14.81	91.38	0.37	0.28	-46	-7.3	0.5±0.5	-0.29	Na-Cl-HCO3
HB	58.1	7.58	2860	1448	385.80	13.12	109.90	1.64	73.69	112.90	0.00	674.00	5.03	69.70	0.53	4.19	-41	-6.2	0.7±0.5	-0.31	Na-Ca-Cl
SZ	83.5	7.54	16521	8460	2248.00	117.90	747.00	7.23	184.30	78.10	0.00	4937.00	2.04	117.92	2.93	21.38	-35	-5.5	0.4±0.5	-0.25	Na-Ca-Cl
MJ	80.0	7.23	22783	11452	2936.00	196.70	1109.00	14.30	188.70	70.17	0.00	6775.00	1.66	130.69	5.93	32.26	-30	-4.5	0.6±0.5	-0.24	Na-Ca-Cl
HQW	75.4	7.58	13540	6874	1833.00	93.27	5776.00	15.21	198.60	103.70	0.00	3939.00	2.49	92.38	3.93	18.23	-36	-5.7	0.5±0.5	0.29	Ca-Na-Cl
ZHY	58.5	7.83	12494	6354	1748.00	65.24	370.60	96.81	453.40	213.60	0.00	3344.00	3.26	45.88	1.72	8.19	-34	-5.2	0.7±0.6	-0.27	Na-Cl

Chemical compositions are expressed in mg/L, Temperature in °C, EC in μS/cm, ^{3}H in Unity Tritium (TU), stable isotopes in the conventional δ notation in ‰;

CBE (%) = $(\sum cations - \sum anions) / (\sum cations + \sum anions)$.

4. Results and discussion

4.1 Physicochemical characteristics

The physicochemical parameters such as temperature, pH, total dissolved solids (TDS), electrical conductivity (EC) are listed in Table 2. Major anion and cation concentrations are used to determine the hydro–geochemical facies, evaluating potential water–rock interactions and reservoir temperatures. The inland and coastal areas of the PRD region display water pH values range of 7.38−9.33 (mean value at 8.2) and 7.23−8.58 (mean value at 7.7), respectively. It is observed that moderately and slightly alkaline correspond to inland and coastal geothermal waters in nature, respectively. The higher the amount of dissolved gases are in the geothermal systems, the lower the pH value will be (Judit et al., 2015). Therefore, this probably implies a great many of dissolved gases (e.g., SO_2) existing in coastal waters.

The electrical conductivity obtained from inland waters vary from 408 to 2486 μS/cm (mean 969.6 μS/cm), while coastal hot waters vary from 1014 to 22783 μS/cm (mean 9141.8 μS/cm). TDS contents of hot waters of the PRD region range widely, from 216 mg/L to 1336 mg/L for inland thermal waters (mean 497 mg/L) and from 520 mg/L to 11452 mg/L for seaside thermal waters (mean 4640 mg/L), respectively.

General trends demonstrate that geothermal water samples with higher temperatures display higher EC and TDS. As representatives of thermal waters from two different geographical settings, sample MJ exhibits highest EC, TDS and lowest pH value, in contrast, hot spring water YFX shows the lowest EC, TDS, and the highest pH value. High EC values can be caused by high concentrations of dissolved minerals in water and can be attributed to high levels of various anions and cations (Fatta et al., 1999; Zainal et al., 2016). Higher TDS values reflect longer circulation path and residence time (Belhai et al., 2016), and also suggest the mixing of seawater in the coastal geothermal waters.

The measured surface temperatures of inland and coastal thermal waters in the PRD region range from 36.5−93.0 °C and 58.1−86.9 °C, an average temperature for 58.9 °C and 71.6 °C, respectively. The highest temperature (93.0 °C) is measured in HR thermal well of 3000m depth of inland area, which is considered as the hottest thermal water in Guangdong. Surface temperatures indicate the circulation depth, time of circulation and regional geothermal gradients (Grasby and Hutcheon, 2001; Zainal et

al., 2016). Therefore, deeper aquifers, long circulation path and long residence time are probably responsible for coastal thermal waters with higher temperature.

4.2 Hydrogeochemical characteristics

4.2.1 Classification of thermal waters

The composition of groundwater can be dependent on many factors, of which temperature–dependent reactions between host rocks and water, flow paths and residence time are assumed to be a major factor (Davraz, 2008). Leaching, mixing, boiling, and cooling processes also play an important role on the final composition of thermal waters (Sharifi et al., 2016; Warner et al., 2013). The classification of thermal waters was made according to the principles of International Association of Hydrogeologists (IAH, 1979). And total equivalents of cations and anions were taken as 100%, and ions greater than 20% (meq/L) were considered in the classification. AquaChem 4.0 of Waterloo-Hydrogeologic was used to evaluate their geochemical properties (Waterloo, 2014).

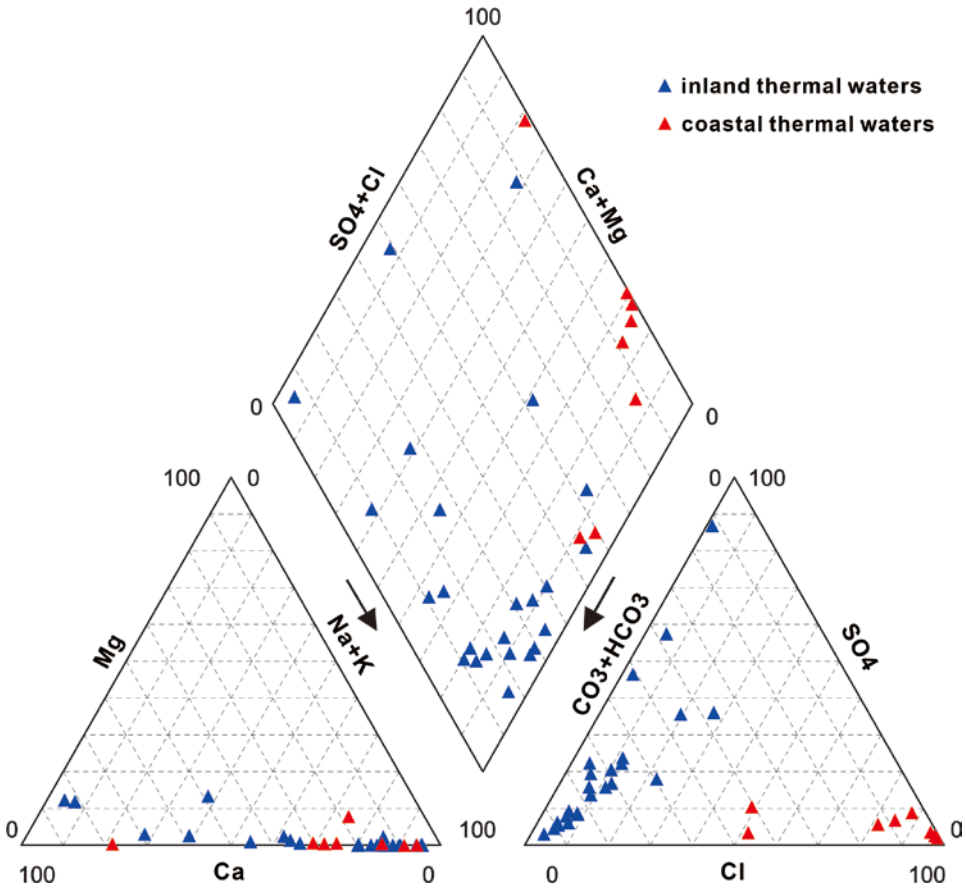

Fig. 4 Piper diagram for the studied geothermal water samples from the PRD region

The major ion concentrations are plotted on the Piper diagram (Piper, 1944) and

illustrated in Fig. 4. Geothermal waters in the PRD region can be mainly divided into four types: (1) sulfate dominated (e.g., Ca–Na–SO_4, Ca–HCO_3–SO_4, Ca–Na–HCO3–SO4), (2) chloride dominated (e.g., Na–Cl, Ca–Na–Cl), and (3) bicarbonate dominated (e.g., Na–HCO_3, Ca–Na–HCO_3, Na–Ca–SO_4–HCO_3). Inland and coastal geothermal waters have extremely varied compositions, with very distinct geochemical features. Thermal waters from inland are mainly of bicarbonate dominated type and sulfate dominated type, whereas the coastal thermal waters are mostly of chloride types. As shown in Table 2 and Fig. 4, the coastal thermal waters reflect simpler hydrochemistry, and the inland waters vary greatly, and are thus more complex in chemistry.

Concentrations of sodium and bicarbonate about the inland waters vary from 6.26 to 314.50 mg/L and 43.93 to 634.60 mg/L, respectively. The dissolved silica concentrations of inland waters range from 52.10 mg/L to 173.23 mg/L. Potassium and magnesium are characterized by the relatively low concentration values. Some inland waters (BS and SS) are enriched in calcium and bicarbonate and the content of Ca^{2+} and HCO_3^- reaches up to 154.2 mg/L and 530.9 mg/L, indicating that carbonate dissolution and water–rock interaction with Carboniferous and Jurassic carbonate dominant rocks play a significant role along the transport of these waters. The lower temperature of BS and SS, compared to other inland geothermal waters, can be correlated to heavy rain, indicating the result of surface water mixing and dilution along with its upward movement (Afsin et al., 2014). Most of those calcium-enriched waters also include sulfate (up to 494.8 mg/L). It is probably due to the result of dissolution of gypsum. The clastic rocks have been found to be interbedded with gypsiferous salts (GBGMI, 1988). Likewise, strontium contents ascend with the increase of calcium concentrations because this element intimately associates with calcium and circulates in regional gypsum aquifer (Minissale et al., 1997).

The coastal waters display a range of dominant concentrations of sodium and chloride with a range from 132 up to 2936 mg/L, and from 169.79 up to 6775 mg/L, respectively. The dissolved silica concentrations of coastal waters vary from 45.88 to 130.69 mg/L. Compared with inland samples, coastal waters exhibit significant increase in sulfate content (with the mean value at 151.6 mg/L). This can be explained by seawater intrusion along the coastal parts of the aquifers. The enrichment of sulfate in thermal waters near the coastline is generally either due to seawater mixing or to dissolution of evaporite minerals deposited under a marine environment (Fara et al., 1999). Sodium and potassium concentrations in coastal thermal waters are very high,

mostly indicating seawater involvement (Baba et al., 2019).

The HCO_3–SO_4–Cl diagram (Fig. 5) also can be used to distinguish a number of different types of thermal waters (Chenaker et al., 2018) and explain a probable mixture between thermal water from geothermal system and cold groundwater recharged by meteoric water (Hernandez and Wurl, 2017). This diagram used for the classification of thermal waters is mainly based on major anion concentrations. Almost all the inland

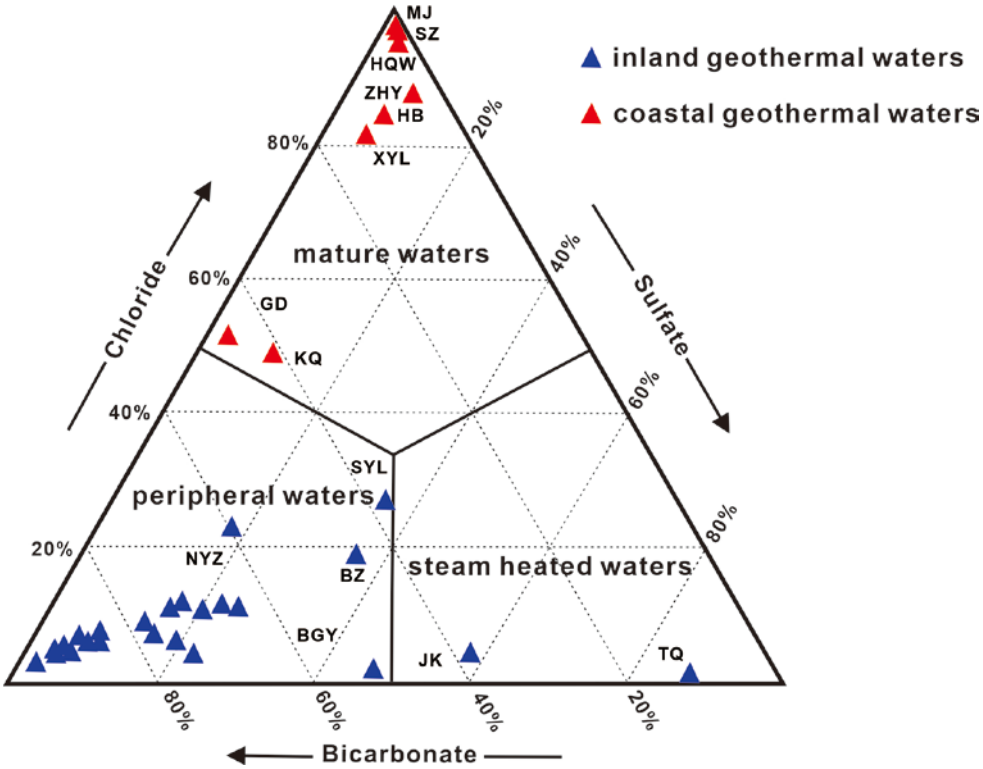

Fig. 5 HCO_3–SO_4–Cl ternary diagram for the geothermal waters from the PRD region

hot waters lie on the peripheral waters field (HCO_3) in this diagram, which can be explained as these inland geothermal waters influenced by surface waters enrichment in this anion (HCO_3). The coastal thermal waters with higher temperature plot in the mature waters field (Cl), suggesting deeper circulation (Chenaker et al., 2018). Combined with Piper diagram, coastal thermal waters near the chloride corner also indicated seawater feeding. Inland waters JK and TQ are located in the field of steam heated waters. It is noteworthy that hot waters JK and TQ have highest sulphate contents (494.80mg/L, 243.20mg/L, respectively) among geothermal waters. This probably can be interpreted as common ion effect (Yang et al., 2019b). The dissolution of sulfate minerals leads to carbonate precipitation and then CO_2 is released from the geothermal system. This suggests that the steam-heated process (most likely CO_2) controls the composition of hot waters JK and TQ.

4.2.2 High fluoride contents

It should be noticed that the concentrations of fluoride (with a mean value of 7.81 mg/L) in almost all of the samples in the study area are above the maximum tolerance limit (1.5 mg/L) recommended by the World Health Organization (WHO, 2004). In general, there is a negative correlation between calcium and fluoride concentration (Handa, 1975). As shown in Table 2, inland or coastal thermal waters with higher contents of calcium tend to have lower concentrations of fluoride in this region. The fluorite, apatite, and fluorapatite in the granites are considered the main origins of fluoride in the groundwater owing to water-rock interactions in alkaline aquifers (Fantong et al., 2010; Handa, 1975). Concentrations of fluoride progressively rise with increasing degrees of water–rock interactions (Saxena and Ahmed, 2001; Yurteri and Simsek, 2017). Besides, the descending order of fluoride concentrations in groundwater is recorded in granitic rocks, complex rocks, volcanic rocks and sedimentary rocks (Chae et al., 2007). In the study area, a wide distribution of Ordovician to Cretaceous granitic rocks indicates that the provenance of fluoride in thermal waters is associated with the mineral composition of granitic rocks. In addition, negative SI values of gypsum and anhydrite and positive SI values (see Table 4) of calcite from geothermal waters in the PRD region are similar to those values in the thermal waters from SEC suggested by (Yang et al., 2019b), which can be explained by the common ion effect. Namely, dissolution of gypsum and/or anhydrite forces calcite precipitation, which has been found in many carbonate hydrothermal systems (Yang et al., 2017; Yang et al., 2019a). The precipitation process lowers the Ca^{2+} concentration in the geothermal waters, which gives rise to unsaturation or sub–saturation of fluorite mineral (CaF_2) in geothermal systems, and thereby geothermal waters show high concentrations of fluoride.

4.2.3 Relations between Cl and other components

Chloride is considered an effective tracer for the origin of fluids because it displays a relatively conservative behavior with a minimum of water–rock interaction (Michard, 1990; Panno et al., 2006). The relationship between Cl and other components of thermal waters including EC, Na, K, Mg, Li, SiO_2, SO_4 and HCO_3 is illustrated in Fig. 6. In this study, few corrections between chloride and these major components are displayed among the inland hot waters. On the contrary, there are strong positive correlations between Cl and EC, Na, K, and Li, and slight positive correlations between Cl and Mg,

SO_4, and SiO_2 among the coastal hot waters. However, there is negative correlation between Cl and HCO_3 in the coastal thermal waters.

Linear correlations between Cl and Na, K, Li, SO_4, and EC observed in coastal thermal waters (Fig. 6) are considered an indicator of the contribution of seawater and dilution of thermal waters (Alçiçek et al., 2016; Alçiçek et al., 2018; Alçiçek et al., 2019b; Avsar et al., 2016; Bozdağ, 2016; Gemici and Filiz, 2001; Gueroui et al., 2018;

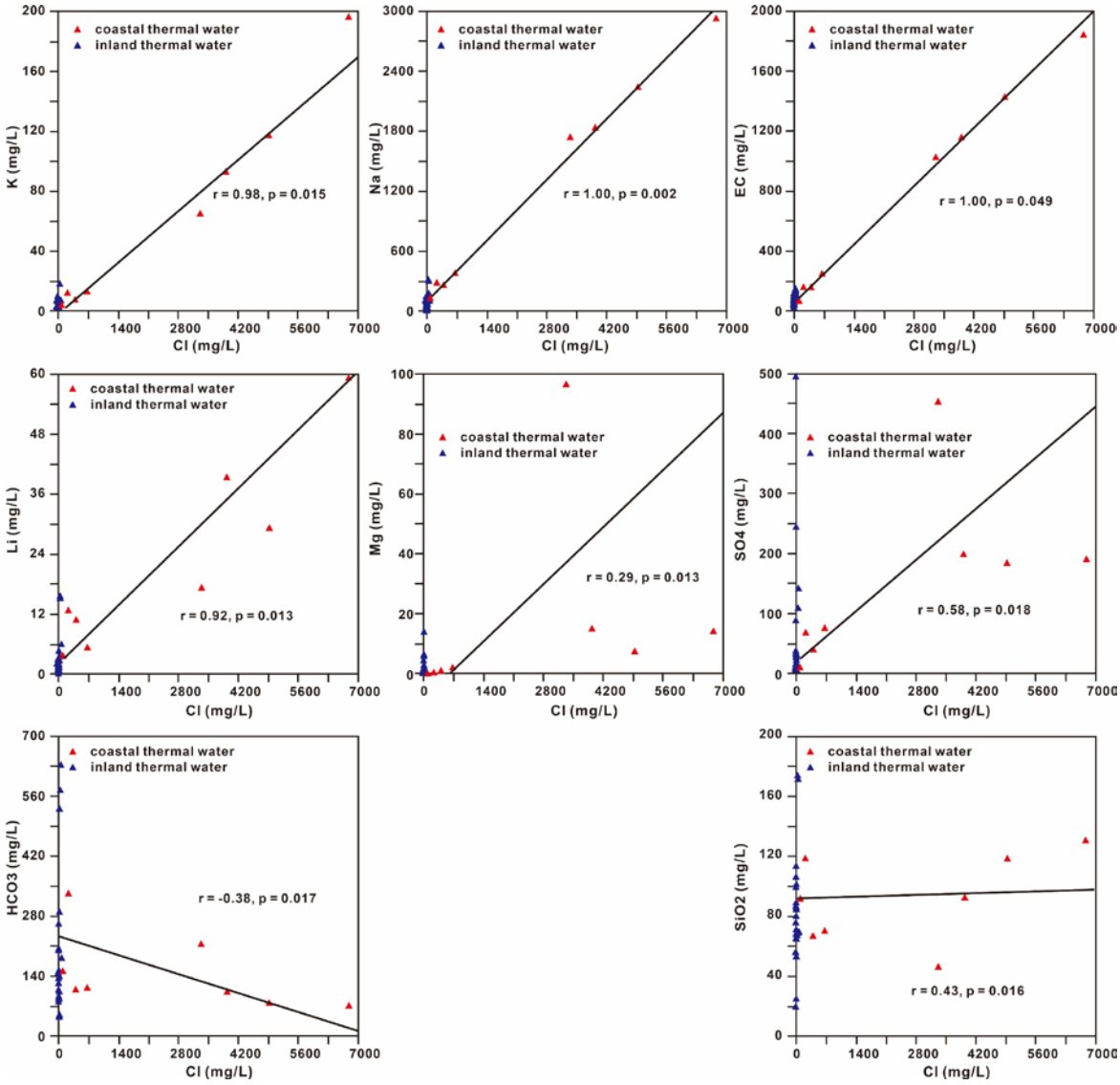

Fig. 6 Relations between chloride and other components in geothermal waters

Tarcan and Gemici, 2003). Due to the high proportions of seawater mixing, Cl and Na concentrations of coastal thermal waters are high. The contributions of seawater lead to an increase in the Cl concentrations but a decrease in the concentrations of HCO_3 in the coastal thermal waters. Costal geothermal water enrichment in chloride generally has higher temperature, and increasing temperature causes an increase in SiO_2 (Tarcan and

Gemici, 2003). Mg is usually incorporated into secondary alteration minerals caused by ion exchange reactions, which results in relatively low Mg levels (Nicholson, 1993), and hence, a negative correlation is expected between Cl and Mg. However, a positive correlation between Mg and Cl indicates that the ascending thermal water is mixed with cold seawater (Fig. 6). According to the relations of the constituents, it is suggested that the initial thermal water near the coastline is a mixture of seawater.

4.3 Oxygen and hydrogen isotopes

4.3.1 Stable isotopes

In this study, $\delta^{18}O$ and $\delta^{2}H$ ratios are also measured in order to determine the origin of geothermal water, as well as the degree of cold water mixing (Bayram and Şimşek, 2005; Ian D. and Peter, 1997). The $\delta^{2}H$ and $\delta^{18}O$ values of thermal waters, rainwater, seawater and river waters from the study area are shown in Table 2. The Hong Kong meteoric line is considered to be the representative of Local Meteoric Water Line (LMWL) with the following equation: $\delta^{2}H = 8.1\ \delta^{18}O + 11.4$ (Wang and Jiao, 2012).

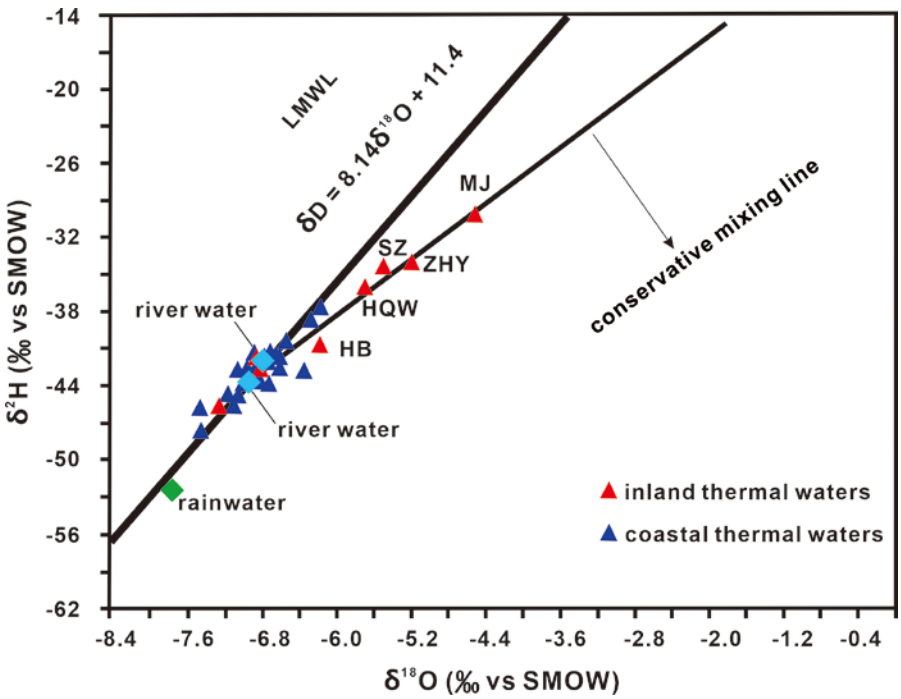

Fig. 7 $\delta^{18}O$–$\delta^{2}H$ concentrations of the thermal water samples from the PRD region

The measured $\delta^{18}O$ and $\delta^{2}H$ values from the investigated water samples are plotted and compared with the LMWL in Fig. 7. The isotopic values of thermal water samples show a limited range of variability: between –30‰ and –48‰ for $\delta^{2}H$ and between –5.2‰ and –7.5‰ for $\delta^{18}O$. Thermal waters with depleted isotope composition mainly correspond to inland sampling locations. These hot waters plot along the LMWL,

indicating that inland geothermal waters are recharged by local precipitation. The heavy isotope enriched samples are only observed at the coastal sampling sites, suggesting that the enrichment can be attributed to the influence of seawater. $\delta^{18}O$ and $\delta^{2}H$ ratios for thermal water samples generally increase towards the seawater. Based on this variation trend, a conservative mixing line of coastal waters can be depicted. As illustrated in Fig. 7, the values of $\delta^{2}H$ and $\delta^{18}O$ of coastal thermal waters deviate from the LMWL but are more aligned with the conservative mixing line, indicating that these coastal thermal waters are recharged by a mixture of precipitation and seawater. Thermal waters from coastal areas also show a deviation of $\delta^{18}O$ and $\delta^{2}H$ values from the LMWL, which suggests isotopic exchanges and strong surface evaporation effects of precipitation–seawater mixtures at relatively high temperatures (Alçiçek et al., 2019a; Chen et al., 2016; Truesdell and Hulston, 1980; Wang et al., 2018).

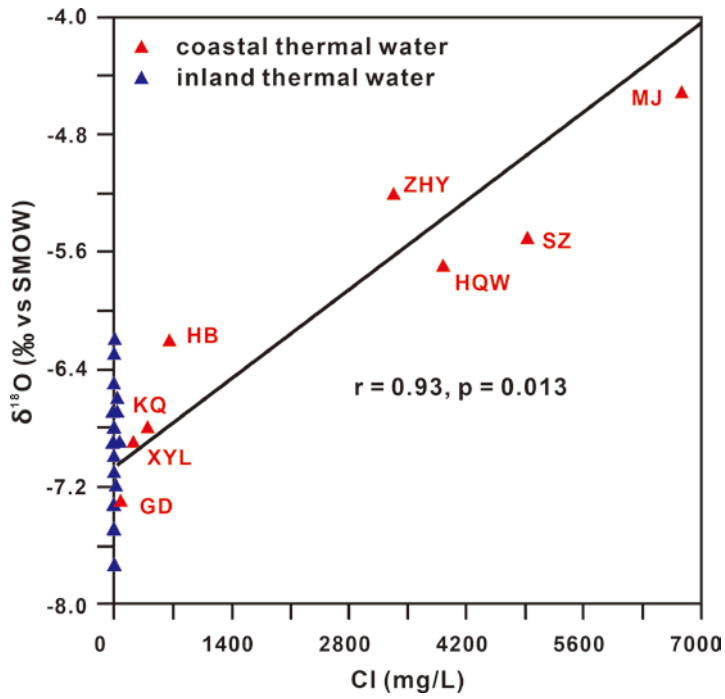

Fig. 8 Relationship between $\delta^{18}O$ and Cl concentrations in coastal thermal waters in study area

For the coastal thermal waters in the study area, both the chloride concentrations and the $\delta^{18}O$ values shows a positive correlation with the salinity (Fig. 8). The extrapolation at zero salinity (zero Cl concentration) gives a $\delta^{18}O$ value of －6.85‰, which is almost identical with the $\delta^{18}O$ values from two cold river waters (average $\delta^{18}O$ = － 6.90‰). This phenomenon suggests that the costal thermal water samples are the mixture of seawater and local cold meteoric water. On the contrary, such correlations are not observed in the inland geothermal water samples.

4.3.2 Tritium

The activity of tritium (^3H) can commonly be used to estimate underground residence time and fluids source of geothermal water (Afsin et al., 2014; Baba et al., 2019; Turali and Simsek, 2017). Groundwater with the lower values for ^3H tends to suggest longer groundwater circulation time or a longer circulation route from recharge to discharge. The tritium content for precipitation during 2005 to 2010, with a mean value of 2.7 ± 1.0 TU in Hong Kong, represents the modern meteoric signal (IAEA/WMO, 2010). It is widely assumed that groundwaters with tritium values less than 1.0 TU are recharged before the 1950s, while waters with values of more than 1.0 TU are modern recharge or mixing with modern water (Clark and Fritz, 1997).

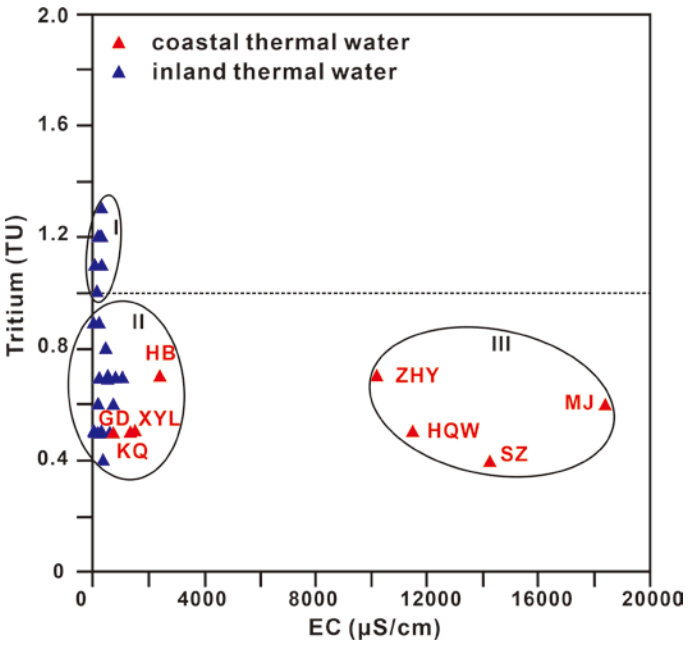

Fig. 9 Variations of tritium vs. EC in thermal waters investigated in this study

The measured tritium concentrations for the PRD thermal waters are in the range from 0.4 to 1.3 TU (Table 2) and three groups of water samples have been identified (Fig. 9). The highest tritium values (AD = 1.1 TU, JBT = 1.2 TU, TS = 1.1 TU, XJ = 1.2, BS = 1.3 TU, BGY = 1.2 TU, group I, Fig. 9) are observed in the inland samples enriched in light isotopes (Fig. 10) and are in accordance with modern precipitation in Hong Kong, likely indicating recent rainwater infiltration. The lower tritium values (SZ = 0.4 TU, MJ = 0.6 TU, HQW = 0.5 TU, ZHY = 0.7 TU, group III) and highest EC values (> 12000 μS/cm) are found in the coastal thermal waters enriched in heavy isotopes, suggesting the recharge of older precipitation and mixing of seawater. The thermal waters with relatively low tritium contents (group II) have relatively low EC

values (Fig. 9) and $\delta^{18}O$ values (Fig. 10), probably reflecting a mixture of old and modern meteoric waters as well as seawater involvement to some extent. And a lack of correlation (group II) between tritium and $\delta^{18}O$ values (Bouchaou et al., 2009; Wang and Jiao, 2012)also can be considered as a symbol of mixture of ^{18}O-depleted modern water with relatively high tritium and deep older thermal waters with lower tritium values and $\delta^{18}O$ values.

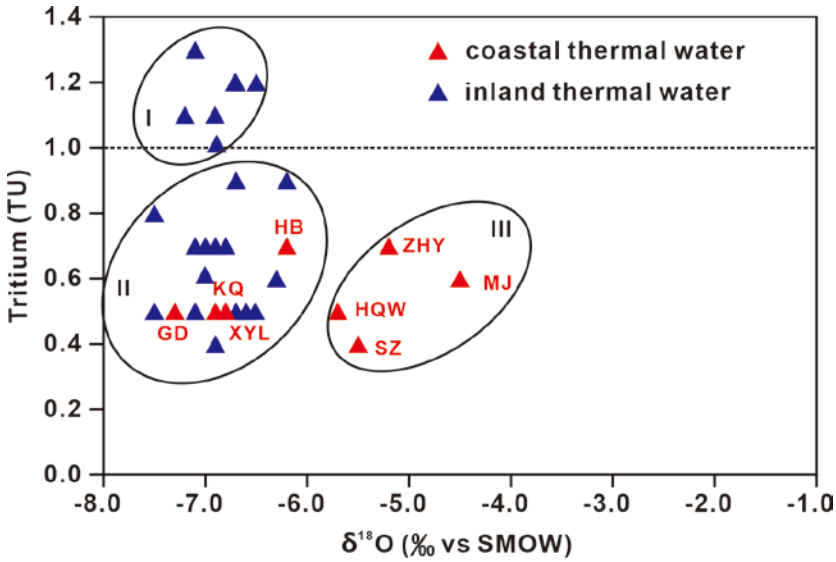

Fig. 10 Variations of tritium vs. $\delta^{18}O$ in thermal waters of the study area

4.4 Geothermometry

4.4.1 Empirical chemical geothermometers

Chemical geothermometers enable the temperature of subsurface reservoir to be estimated, and thus can contribute to the exploration and development of the geothermal resources. Chemical geothermometers are based on temperature–dependent water–mineral equilibria and can provide equilibration temperature (Chenaker et al., 2018; Nicholson, 1993). In this study, some solute geothermometers are applied to geothermal waters from springs and thermal wells. The calculation results of quartz (no steam loss and maximum steam loss), chalcedony, α–cristobalite, β− cristobalite (Fournier, 1977), Na–K (Arnorsson, 1983; Giggenbach, 1988; Nieva and Nieva, 1987), Na–K–Ca (Fournier and Truesdell, 1973a), K–Mg (Giggenbach, 1988), Na–Li (Fouillac and Michard, 1981) and Mg–Li geothermometer (Kharaka and Mariner, 1989) are presented in Table 3.

Temperatures obtained from different silica phases in geothermal waters of the PRD region are listed in Table 3. Reservoir temperatures evaluated by chalcedony, α–

cristobalite, β−cristobalite are lower than temperatures given by quartz. Notably, assessment results from β–cristobalite are unreasonable because the geothermometers give negative values (e.g., BS, SS, BGY) and other values are lower than the measured temperature of thermal waters. Calculations from α–cristobalite geothermometers are close to or lower than the measured surface temperature of geothermal waters. Accordingly, α–cristobalite and β–cristobalite geothermometers are unreliable since water temperature will somewhat tend to increase towards deep reservoirs.

The HR thermal well had been drilled and investigated by Chinese Academy of Geological Sciences in 2018, and the measured temperature from bottom hole at 3000m depth was 132 °C (unpublished data from a report on a geothermal project by Chinese Academy of Geological Sciences). This result is in line with the 147 °C chalcedony geothermometer calculation from sample HR. This also suggests that the actual deep reservoir temperature can be higher. The calculated temperatures using quartz geothermometers (no steam loss and maximum steam loss) vary in the range of 62–170 °C and 67–160 °C, which seems to be unexpectedly high. Compared with the deep reservoir temperature of 132°C in HR geothermal well, 160 °C and 170 °C computed by quartz geothermometers are higher than those by chalcedony. Equilibrium with quartz may be attained at higher temperatures in geothermal systems. Chalcedony rather than quartz controls phase equilibrium at least at temperatures of lower than 180 °C of groundwater systems (Arnorsson, 1983). However, in terms of the water sample BS, SS and BGY, results given by chalcedony geothermometers are even much lower than the measured surface temperature. This phenomenon may be associated with rainwater or surface water because these three samples were collected in the rain and show relatively lower surface temperatures (36.5-42.9 ℃), TDS values (316-756 mg/L), and SiO2 concentrations (19.03-24.34 mg/L) and highest tritium contents (1.2-1.3 TU) in comparison with other inland thermal waters. Plenty of rainwater and surface water mixing with ascending hot water lower SiO_2 concentration in these samples, which leads to incorrect calculations. For the three samples, α–cristobalite, β–cristobalite, Na−K−Ca, K−Mg thermometers give estimations lower than the measured temperatures as well, and Na−K, Na−Li give unexpectedly high results (Table 3). Given these anomalous results, quartz geothermometer (no steam loss) should be identified as a reasonable calculation method of the reservoir temperatures of the water sample BS, SS and BGY, which are 62 °C, 62 °C, and 71 °C, respectively.

Table 3 Temperature results obtained with empirical chemical geothermometers for the PRD region thermal waters (values in ℃)

No	ID	Water Sample Temperature	SiO2					Na-K-Ca	Na-K			K-Mg	Mg-Li	Na-Li	
			a	b	c	d	e	f	g	h	i	j	k	l	m
1	HR	93.0	170	160	147	120	70	153	191	144	161	81	97	97	215
2	ZX	58.1	140	135	114	90	41	98	182	133	152	77	124	58	160
3	BPL	52.9	119	117	90	68	20	73	165	113	134	79	114	52	151
4	HL	93.2	170	160	148	120	71	155	195	148	165	82	94	100	220
5	LZQ	65.8	131	127	103	80	32	78	188	141	158	68	139	79	190
6	LX	51.2	116	115	88	66	18	62	168	116	137	74	131	47	144
7	SH	57.1	129	125	101	78	30	55	161	108	130	74	114	67	173
8	NYZ	61.2	104	105	74	54	7	79	174	124	144	78	104	82	194
9	SQW	54.5	114	113	85	63	16	59	172	121	141	73	118	74	182
10	JS	67.1	128	125	100	77	29	85	141	86	110	74	100	74	183
11	AD	60.1	115	114	87	65	17	67	157	103	125	51	191	61	164
12	JBT	38.6	107	107	77	57	9	58	218	177	189	63	175	70	177
13	TS	78.0	125	122	97	74	26	50	230	192	202	57	212	63	167
14	DP	37.0	104	104	74	53	6	45	207	164	178	58	201	55	155
15	SYL	59.8	117	116	89	67	19	89	169	118	138	76	108	79	190
16	DD	67.2	122	120	94	72	24	96	174	124	143	77	115	66	171
17	BS*	36.5	62	67	29	13	-	35	211	169	182	42	303	43	138
18	SS*	41.9	62	68	30	13	-	12	386	417	371	42	361	88	203
19	XJ	60.9	116	115	88	66	18	42	248	215	220	54	249	49	147
20	BGY*	42.9	71	76	39	22	-	6	335	338	315	39	543	6	86
21	YFX	65.9	136	132	110	86	37	67	179	130	149	72	146	43	138
22	BZ	42.4	138	133	111	87	38	88	166	115	135	76	101	87	201
23	TQ	58.6	129	126	102	79	30	38	214	172	184	52	241	45	142
24	JK	58.9	144	138	118	93	45	69	198	152	168	58	174	80	191
25	KQ	86.9	147	141	121	96	47	130	175	124	144	85	85	91	208
26	XYL	67.6	116	114	87	65	17	87	150	96	119	65	121	87	202
27	GD	63.0	132	129	105	82	33	85	152	98	121	81	93	67	173
28	HB	58.1	118	116	89	67	20	85	159	106	128	66	159	35	126
29	SZ	83.5	147	141	121	96	47	145	186	137	155	84	126	32	123
30	MJ	80.0	153	146	128	102	53	161	202	157	172	86	115	51	150
31	HQW	75.4	133	129	106	82	34	80	184	135	153	76	129	54	154
32	ZHY	58.5	98	99	68	48	1	135	164	112	133	61	194	21	108

"-" represents negative values with respect to this geothermometer

"*" see the discussion of chalcedony geothermometer

a Quartz, no steam loss, $t = [1309/(5.19 - logSiO_2)] - 273.15$ (Fournier, 1977)

b Quartz, maximum steam loss, $t = [1522/(5.75 - logSiO_2)] - 273.15$ (Fournier, 1977)

c Chalcedony, $t = [1032/(4.69 - logSiO_2)] - 273.15$ (Fournier, 1977)

d α–Cristobalite, $t = [1000/(4.78 - logSiO_2)] - 273.15$ (Fournier, 1977)

e β–Cristobalite, $t = [781/(4.51 - logSiO_2)] - 273.15$ (Fournier, 1977)

f Na–K–Ca, $t = \left\{1647/\left[log(Na/K) + \beta\left(log\left(Ca^{1/2}/Na\right) + 2.06\right) + 2.47\right] - 273.15\right\}$

if T>100 °C, β=1/3; if T<100 °C, β=4/3 (Fournier and Truesdell, 1973a)

g Na–K, $t = \{1390/[log(Na/K) + 1.75] - 273.15\}$ (Giggenbach, 1988)

h Na–K, $t = \{933/[log(Na/K) + 0.993] - 273.15\}$ (Arnorsson, 1983)

i Na–K, $t = \{1178/[log(Na/K) + 1.47] - 273.15\}$ (Nieva and Nieva, 1987)

j K–Mg, $\mathrm{t} = \left\{4410/\left[log\left(K/Mg^{1/2}\right) + 14.0\right] - 273.15\right\}$ (Giggenbach, 1988)

k Mg–Li, $\mathrm{t} = \left\{2200/\left[log\left(Li/Mg^{1/2}\right) + 5.47\right] - 273.15\right\}$ (Kharaka and Mariner, 1989)

l Na–Li, $t = \{1000/[log(Na/Li) + 0.389] - 273.15\}$ (Fouillac and Michard, 1981)

m Na–Li, $t = \{1195/[log(Na/Li) + 0.130] - 273.15\}$ (Fouillac and Michard, 1981)

For the cation geothermometers, the highest estimated reservoir temperatures are indicated by the Na–Li geothermometers, whereas the K–Mg geothermometer gives the lowest temperatures. Results for the different cation geothermometers are shown in Table 3. Much lower or higher results can probably be attributed to the hydrogeological conditions failing to match the basic assumptions for their application (Mohammadi et al., 2010).

Temperatures obtained from two Na–Li geothermometers vary in the range of 6–100 ℃ and 86–208 ℃, respectively. The Mg–Li geothermometers give calculated temperatures with a range of 85–534 ℃. However, these results appear to be too low or high for the reservoir temperature. It is because the relatively rapid ion exchange reactions, such as mobile element lithium with clays and zeolites, are controlled by equilibria which is not fulfilled. The Na–Li geothermometer is suitable for estimating the high–temperature reservoirs since they are less affected by dilution (Fouillac and Michard, 1981). Especially in low salinity and enthalpy groundwater systems, lithium concentrations are often less than 1mg/L (D'Amore et al., 1987), thus the Na–Li and Mg–Li geothermometers results are less reliable, and hence they have not been taken into account.

Na–K geothermometers give some unexpectedly high temperatures, ranging up to ~420 ℃, which appear to be much higher than possible and incorrect for mixing waters in this study. This is probably due to leaching and other secondary processes (e.g., mixing) rather than the chemical equilibrium mainly controlling cation contents in these geothermal waters (Alçiçek et al., 2016; Mutlu and Gulec, 1998; Wang et al., 2015). The application of this geothermometer, especially for diluted thermal waters or geothermal systems below 150 ℃, possibly results in overestimated temperatures (D'Amore et al., 1987; Henley et al., 1985).

The estimation of reservoir temperatures, reaching up to 166 ℃, can be obtained by the Na–K–Ca chemical geothermometer. However, the calculated temperatures using the Na–K–Ca geothermometer are close to or even lower than examined surface temperature (e.g., TS and BS), showing that thermal waters are strongly affected by dilution. It should be interpreted as hot waters coming from deep aquifers or reservoirs

at more shallow depth or lower temperatures (D'Amore et al., 1987; Fournier and Truesdell, 1973b). Thus, the geothermometer cannot be reliable for the calculation of reservoir temperatures.

The reservoirs temperatures computed by K–Mg geothermometer range from 40–86 ℃, and similarly some cases are approaching and even lower than springs outlet temperatures (e.g., HR, HL). This empirical method can be applied to the situation in which dissolved calcium and sodium are not in equilibrium with minerals (Giggenbach et al., 1983), reflecting very low magnesium contents in the groundwaters or magnesium attaining equilibrium at shallower levels (Mutlu and Gulec, 1998; Pirlo, 2004), and therefore K–Mg geothermometer cannot be considered a good indicator of deep temperatures.

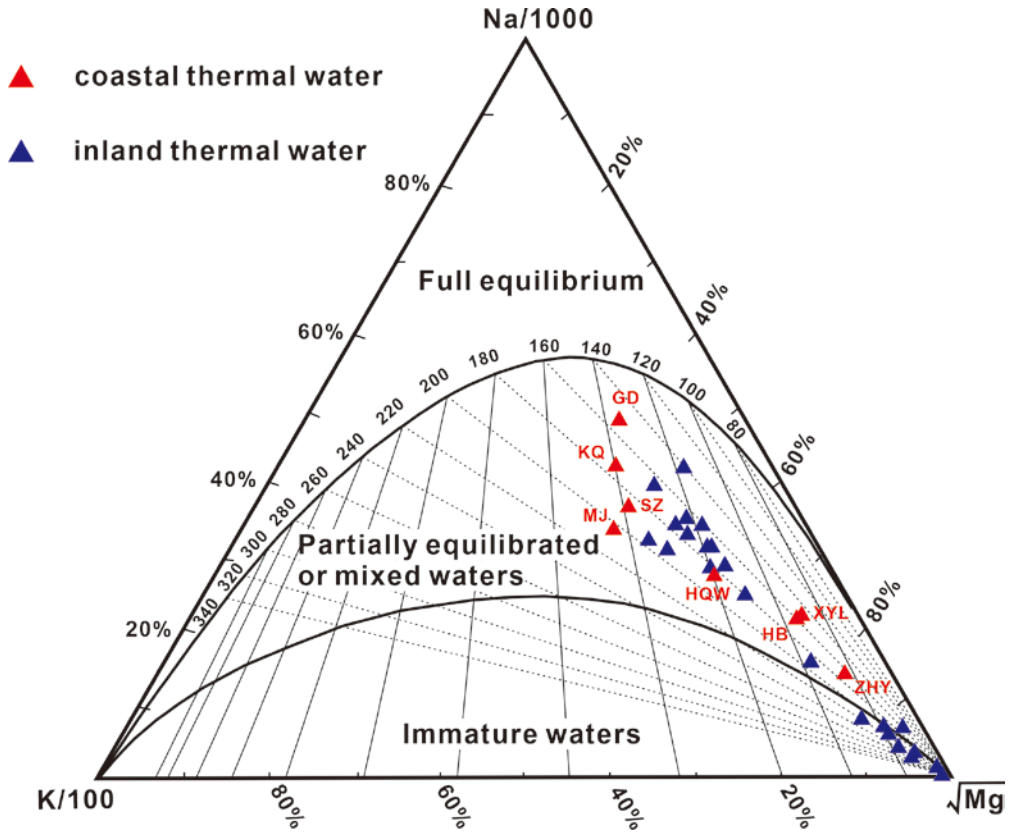

Fig. 11 Distribution of thermal waters from the study area in the Na–K–Mg ternary diagram

The Na–K–Mg ternary diagram (Giggenbach, 1988) based on the chemical equilibrium of major cations is used to determine the applicability of chemical geothermometers, determine deep reservoir temperatures and recognize waters that

have attained equilibrium with wall rocks by using relative Na/1000, K/100 and $Mg^{1/2}$ contents (Yurteri and Simsek, 2017). As can be seen in the ternary diagram (Fig. 11), all thermal water samples plot in the non-equilibrium field, indicating that none of these waters has attained full equilibrium between water and rocks. This is probably due to the influence of re-equilibrium and/or strong dilution and seawater intrusion into thermal waters. However, it seems that the degree of equilibrium in coastal thermal waters is higher than that in the inland waters, indicating coastal cases have mixed less cold water. Therefore, these cation geothermometers are not likely to yield practical reservoir temperatures. Overall, chalcedony geothermometer is more applicable and appropriate to estimate the reservoir temperatures for the study area in comparison to quartz and cation geothermometers.

4.4.2 Mineral saturation states

Calculation about mineral equilibrium or saturation has turned out to be another helpful approach in predicting the presence of reactive minerals (Guo et al., 2017; Mohammadi et al., 2010). The saturation index (SI) for diverse minerals in both thermal waters was calculated at the measured discharge temperature by using the Aquachem-Phreeqc computer program (Parkhurst and Appelo, 1999). Calculated saturation indices for thermal waters from study area are reported in Table 4. A negative or positive SI of minerals indicates undersaturation or oversaturation, and SI values equal to zero imply saturation. As shown in Table 4, all thermal waters are undersaturated with respect to anhydrite, amorphous silicon, gypsum, celestite, sepiolite and strontianite, chrysotile, and dolomite. Saturation indices of chalcedony tend to be closer to zero value than any other minerals as a whole, suggesting the applicability of chalcedony geothermometry in assessing reservoir temperatures discussed above. Due to the saturation indices of fluorite converging to zero, almost all thermal waters are saturated with respect to fluorite with the exception few samples (e.g., SQW, SS). These waters are oversaturated with respect to calcite, aragonite, quartz, chalcedony and talc which occur as the scale formation.

Table 4 Saturation indices with respect to various minerals at the discharge temperature of thermal waters

Sample ID	Anhydrite	Aragonite	Calcite	Celestite	Chalcedony	Chrysotile	Dolomite	Fluorite	Gypsum	Quartz	Sepiolite	SiO2(a)	Strontianite	Talc
HR	-1.79	0.77	0.87	-2.08	0.27	0.69	0.20	-0.18	-2.30	0.51	-1.64	-0.36	-0.61	5.68
ZX	-2.74	0.24	0.37	-2.49	0.44	-3.65	-1.03	0.11	-2.74	0.77	-3.03	-0.30	-0.83	1.30
BPL	-2.78	0.07	0.20	-2.53	0.31	-6.98	-2.16	0.11	-2.74	0.66	-5.30	-0.44	-1.01	-2.33
HL	-2.14	1.10	1.21	-2.19	0.17	3.76	1.00	-0.33	-2.52	0.52	0.65	-0.38	-0.08	8.67
LZQ	-2.61	0.58	0.69	-2.69	0.29	-1.76	-0.08	0.02	-2.68	0.60	-2.25	-0.43	-0.79	2.97
LX	-3.29	-0.28	-0.15	-3.10	0.31	-7.83	-2.73	-0.22	-3.24	0.67	-5.80	-0.44	-1.43	-3.19
SH	-3.16	0.27	0.39	-3.19	0.35	-6.03	-1.38	0.02	-3.15	0.69	-4.72	-0.29	-1.09	-1.26
NYZ	-3.05	0.39	0.51	-2.76	0.02	-1.68	-1.27	-0.49	-3.08	0.35	-2.50	-0.71	-0.63	2.47
SQW	-4.19	0.35	0.48	-4.28	0.21	-2.89	-1.43	-3.89	-4.16	-0.56	-2.79	-0.54	-1.07	1.58
JS	-3.18	0.30	0.42	-3.11	0.12	0.04	-1.20	-0.46	-3.27	0.43	-1.63	-0.60	-0.90	4.44
AD	-2.77	0.45	0.57	-2.31	0.18	2.99	0.70	0.13	-2.79	0.51	0.91	-0.56	-0.40	7.44
JBT	-3.06	-0.14	0.00	-2.94	0.36	-5.53	-1.49	-0.85	-2.91	0.75	-3.78	-0.43	-1.39	-0.93
TS	-3.21	0.55	0.67	-3.83	0.06	3.86	0.18	-1.34	-3.41	0.35	0.77	-0.63	-1.27	8.23
DP	-2.73	-0.17	-0.04	-2.84	0.35	-6.10	-1.51	0.01	-2.57	0.75	-4.12	-0.45	-1.65	-1.55
SYL	-1.91	0.39	0.51	-1.80	0.23	-3.21	-0.86	0.17	-1.93	0.56	-3.13	-0.50	-0.81	1.43
DD	-3.87	0.18	0.30	-3.81	0.04	0.65	-1.31	-0.93	-3.96	0.35	-1.10	-0.68	-1.03	4.89
BS	-3.05	0.84	0.97	-2.51	-0.10	1.36	1.63	-0.19	-2.89	0.29	0.12	-0.90	0.02	5.00
SS	-2.38	0.84	0.97	-2.90	-0.23	-3.36	1.39	-1.46	-2.25	0.25	-3.27	-0.92	-2.04	0.28
XJ	-2.12	0.50	0.62	-2.17	0.22	-0.65	0.19	-0.12	-2.15	0.55	-1.49	-0.51	-0.86	3.89
BGY	-1.78	0.44	0.57	-1.56	-0.05	-0.84	0.58	-1.42	-1.66	0.33	-1.48	-0.83	-0.71	2.99
BZ	-3.36	-0.02	0.12	-3.54	0.39	0.14	-1.85	-0.21	-3.24	0.76	-0.08	-0.40	-1.56	4.83
TQ	-0.74	0.46	0.58	-0.61	0.35	-0.56	0.01	0.43	-0.75	0.69	-1.13	-0.39	-0.73	4.22
JK	-1.31	0.70	0.83	-1.15	0.46	0.47	0.71	0.12	-1.32	0.79	-0.27	-0.28	-0.45	5.47

KQ	-2.13	0.68	0.79	-2.16	0.22	-0.99	-0.43	-0.19	-2.44	0.49	-2.44	-0.45	-0.50	3.78
XYL	-1.99	0.57	0.69	-1.87	0.13	-2.15	0.14	-0.05	-2.08	0.45	-2.82	-0.58	-0.58	2.29
GD	-3.29	0.31	0.43	-3.08	0.27	-2.12	-1.68	0.21	-3.34	0.60	-2.43	-0.45	-0.78	2.55
HB	-1.71	0.35	0.47	-1.34	0.27	-2.35	-0.38	0.12	-1.71	0.60	-2.45	-0.47	-0.60	2.26
SZ	-0.74	0.87	0.98	-0.69	0.29	1.56	0.32	-0.47	-1.01	0.56	-0.54	-0.39	-0.26	6.44
MJ	-0.73	0.63	0.74	-0.64	0.38	0.33	0.01	-0.56	-0.96	0.66	-1.11	-0.31	-0.48	5.36
HQW	-0.43	1.45	1.56	-1.27	0.27	1.70	1.01	0.11	-0.61	0.57	-0.24	-0.42	-0.62	6.49
ZHY	-0.89	1.09	1.21	-0.76	0.09	3.55	2.35	-0.18	-0.90	0.42	1.17	-0.65	-0.10	7.81

Saturation indices evaluated by using the Aquachem-Phreeqc computer program

The equilibrium state between groundwater and minerals can also be identified as a temperature-dependent function, and saturation index, therefore, can be used as a very helpful method for evaluating reservoir temperature by plotting temperature versus saturation index (SI) (Avsar et al., 2016; Reed and Spycher, 1984). The intersection of the SI curves at zero saturation index can be assumed to give the equilibrium temperature that is most likely, especially when the saturation indices with respect to a group of minerals converge to zero (D'Amore et al., 1987). By using this computer program, the saturation indices of common hydrothermal minerals were recalculated iteratively for each site for temperatures ranging between 25 and 200 °C.

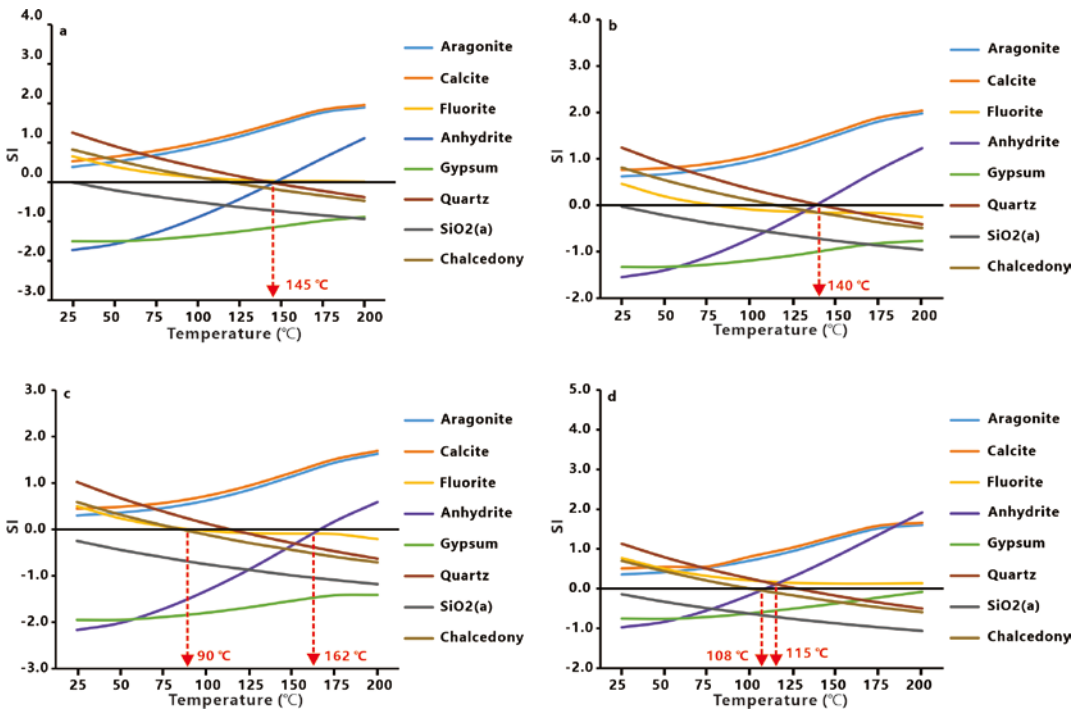

Fig. 12 Temperature vs. SI diagrams for JS (a), JK (b), SYL (c) and TQ (d) as representatives of inland thermal waters.

Fig. 12 shows SI with respect to each mineral versus temperature for inland thermal water samples JS, JK, SYL and TQ as representatives. For the JS thermal water (Fig. 12a), the SIs with respect to anhydrite and quartz minerals exactly converge to zero at 145 °C. For the sample JK (Fig. 12b), anhydrite and quartz minerals are saturated at temperature of 140 °C. The sample SYL (Fig. 12c) reaches the state of equilibrium at the temperatures between 90−162 °C. The SI trend curves for TQ thermal water (Fig. 12d) with respect to anhydrite and chalcedony are in equilibrium at 108 °C and quartz, fluorite, and anhydrite minerals get close to zero line at 115 °C.

Fig. 13 shows the variation of saturation indices for coastal thermal waters. As a representative, similarly, for the sample ZHY quartz and anhydrite are saturated at temperature of 113 °C (Fig. 13a). In Fig. 13b, for the sample SZ, chalcedony and anhydrite minerals tend to be near to zero at 125°C and the equilibrium between aqueous solution and quartz and anhydrite minerals is reached at 134°C. In Fig. 13c, chalcedony and anhydrite minerals approach zero at 125 °C for the MJ thermal water. In the sample HQW (Fig. 13d), anhydrite and chalcedony minerals reach the state of equilibrium at the temperature of 108 °C.

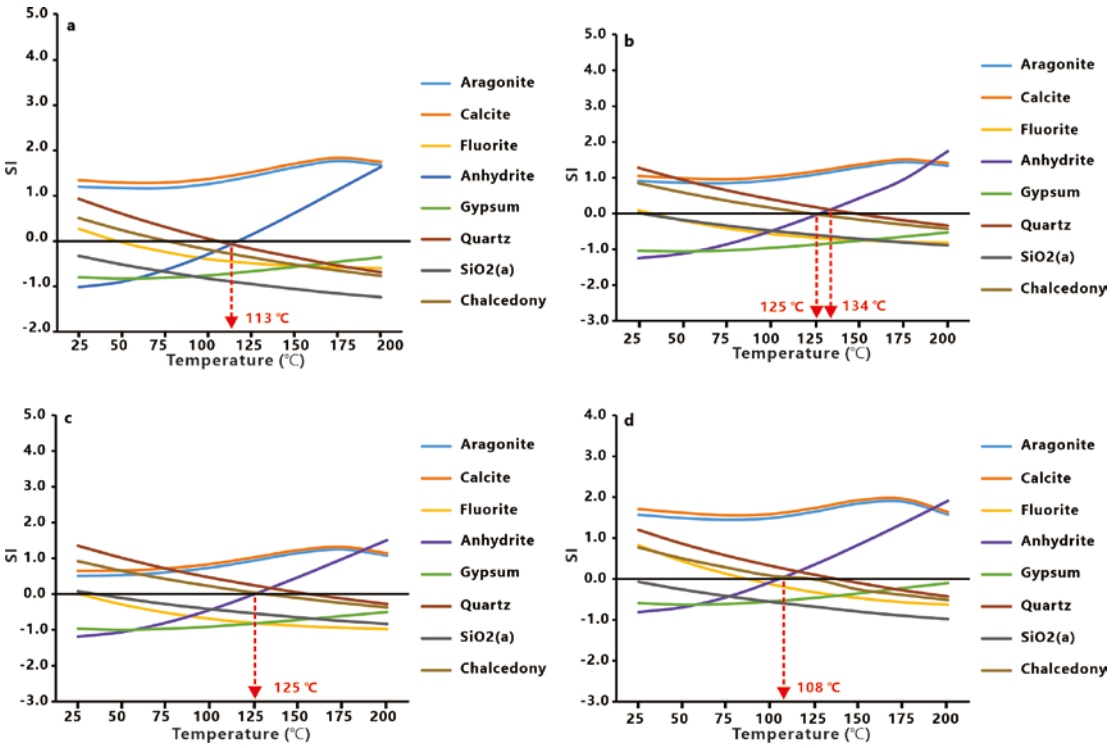

Fig. 13 Temperature vs. SI diagrams for ZHY (a), SZ (b), MJ (c) and HQW (d) as representatives of coastal thermal waters.

As can be observed in Fig. 12 and Fig. 13, more minerals in representative cases do not intersect each other at the equilibrium line, and the intersections are below the equilibrium line of these minerals at various temperatures, which probably indicates a mixing process between geothermal waters and groundwaters or different temperature fluids (Sharifi et al., 2016; Tarcan and Gemici, 2003). It is noteworthy that positive SI values for carbonate minerals (calcite and aragonite) observed throughout the temperature range indicate a supersaturation phenomenon, which is associated with the effects of extensive CO_2 degassing forcing carbonate minerals precipitation in almost all waters (Delalande et al., 2011; Guo et al., 2017; Luo et al., 2017; Pang and Reed,

1998; Pastorellia et al., 1999; Reed and Spycher, 1984). These previous studies suggest that degassing of CO_2 interferes with equilibrium temperatures and that the last re-equilibration before the discharge is likely to be attained under relatively high CO_2 partial pressure.

Given the influence of mixing processes and CO_2 degassing, these temperatures can be considered to be only broad estimations. The assessment of saturation indices for the minerals shows reservoir temperatures between 90 and 162 °C for inland thermal waters and between 108 and 134 °C for coastal thermal waters, even though thermal waters in the PRD region are nonequilibrium waters.

Besides, the saturation indices with respect to the combination of anhydrite and chalcedony minerals can also be used to evaluate the equilibrium temperature of thermal waters (Alçiçek et al., 2016). Likewise, equilibrium temperatures can be estimated if SIs of both minerals cluster and get close to zero at the same temperature. Inland thermal waters (HL, HR, SS, JK, SYL, TQ, and HB) and coastal thermal waters (XYL, SZ, MJ, HQW, and ZHY) are taken into account in this study. The assessments suggest that SI curves of chalcedony and anhydrite are converging to equilibrium line at the temperature ranging 105–154 °C for these inland waters (Fig. 14a) and 104–131 °C for these coastal waters (Fig. 14b). Overall, temperature values estimated by chalcedony/anhydrite are compatible with calculations by chalcedony geothermometers and mineral saturation states and represent more constrained reservoir temperature estimations.

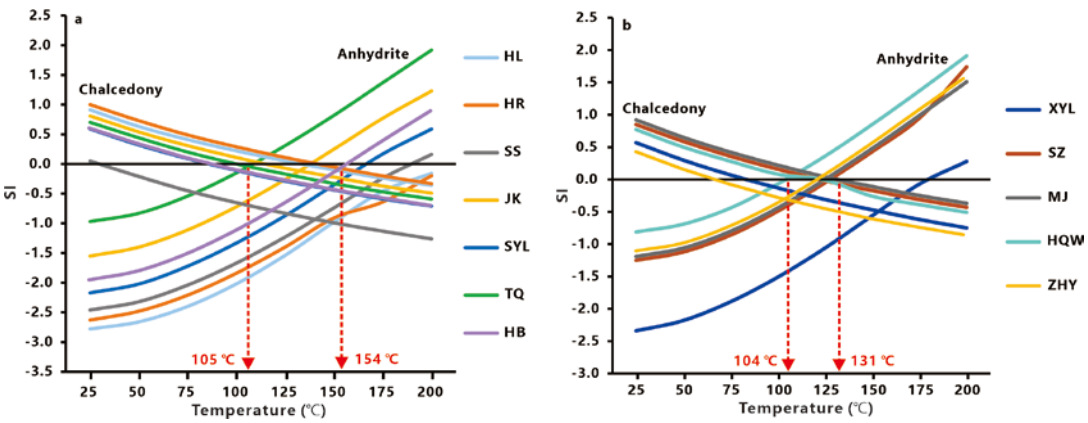

Fig. 14 Temperature vs. variation of saturation indices with respect to anhydrite and chalcedony minerals for inland thermal waters (HL, HR, SS, JK, SYL, TQ, and JS) and coastal thermal waters (XYL, SZ, MJ, HQW, and ZHY)

4.4.3 Mixing models and ratios

The relationships between chloride and other major constituents, isotopic ratios, empirical geothermometers, mineral saturation states and the activity of tritium uniformly confirm the presence of mixing processes in the thermal waters of the PRD region. This indicates that the realistic deep reservoir temperatures can be higher. To evaluate and eliminate the effects of the mixing processes, the silica–enthalpy mixing model (Truesdell and Fournier, 1977) is applied in the thermal waters and this model can also be considered as another approach for reservoir temperature estimation. The inland thermal waters HL, HR, JK, ZX, YFX, TQ, SYL, TS, and JS and coastal waters MJ, GD, SZ, HQW, KQ, HB, XYL, ZHY are selected and involved in this model (Fig. 15 and Fig. 16), and the silica concentrations of these waters are plotted against the corresponding enthalpies (Keenan et al., 1969).

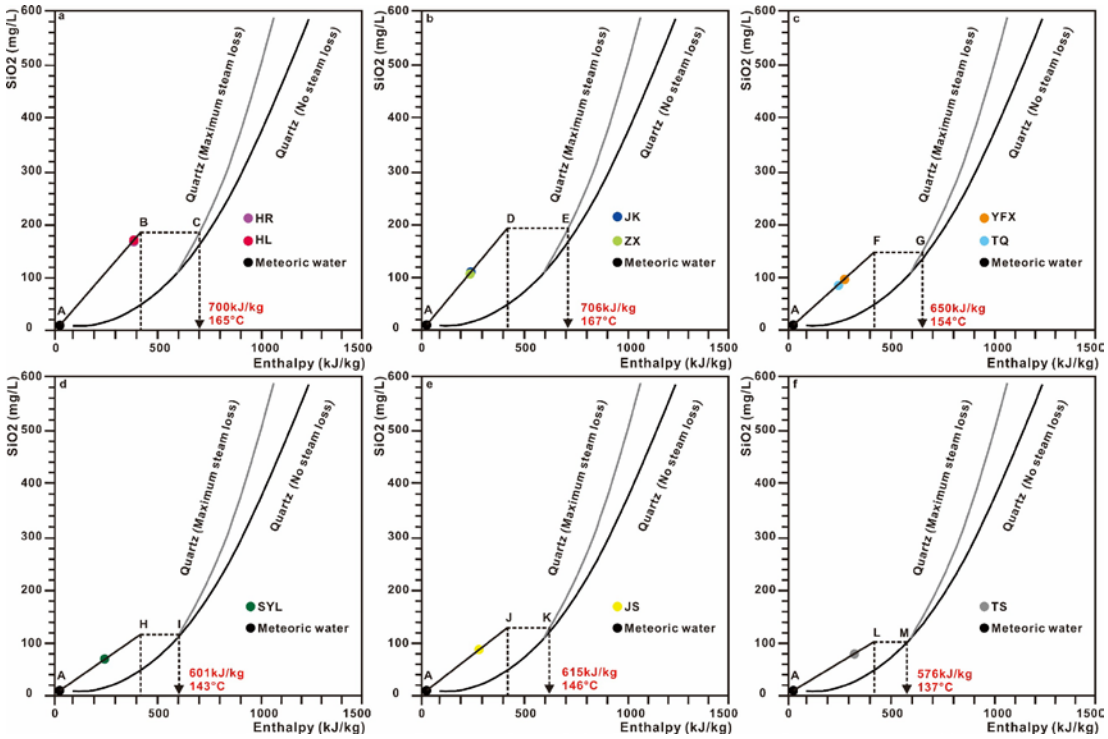

Fig. 15 Silica–enthalpy model for the inland thermal waters HR and HL (a), JK and ZX (b), YFX and TQ (c), SYL (d), JS (e), and TS (f).

Two end member fluids have been presented in this model: a cold water sample (local precipitation) as one end member and inland or coastal thermal water as the other end member. The mixing lines (straight unbroken lines) from cold water (point A) to thermal waters intersect with a vertical broken line drawn at the temperature where boiling is assumed to have occurred (419 kJ/kg, 100°C) at points B, D, F, H, J, and L. From these points broken lines parallel to enthalpy axis intersect the quartz solubility curve (maximum steam loss) at points C, E, G, I, K, and M. For Fig. 16e a straight

unbroken line from cold water to thermal water intersects the quartz solubility curve at point P. The very first point that needs to be made is that two thermal waters plotted on one mixing line (e.g., Fig. 15a) do not mean mixing with each other but a mixing process between one thermal water and one cold water separately. These intersections (C, E, G, I, K, M, and P) indicate reservoir temperatures and enthalpies, giving 700 kJ/kg and 165 °C for HR and HL hot waters (Fig. 15a), 706 kJ/kg and 167 °C for JK and ZX thermal waters (Fig. 15b), 650 kJ/kg and 154 °C for YFX and TQ hot waters (Fig. 15c), 601 kJ/kg and 143 °C for SYL hot fluid (Fig. 15d), 615 kJ/kg and 146 °C for JS geothermal water (Fig. 15e), and 576 kJ/kg and 137 °C for TS geothermal water (Fig. 15f). Likewise, with respect to the coastal waters, this model shows 660 kJ/kg and 156 °C for MJ and GD hot waters (Fig. 16a), 625 kJ/kg and 148 °C for KQ and SZ thermal waters (Fig. 16b), 615 kJ/kg and 146 °C for HB and HQW hot waters (Fig. 16c), 572 kJ/kg and 136 °C for XYL hot fluid (Fig. 16d), and 601 kJ/kg and 143 °C for ZHY thermal water (Fig. 16e). Furthermore, it should be pointed out that these temperatures suggested by the silica–enthalpy mixing model represent the maximum reservoir temperatures of thermal waters before mixing.

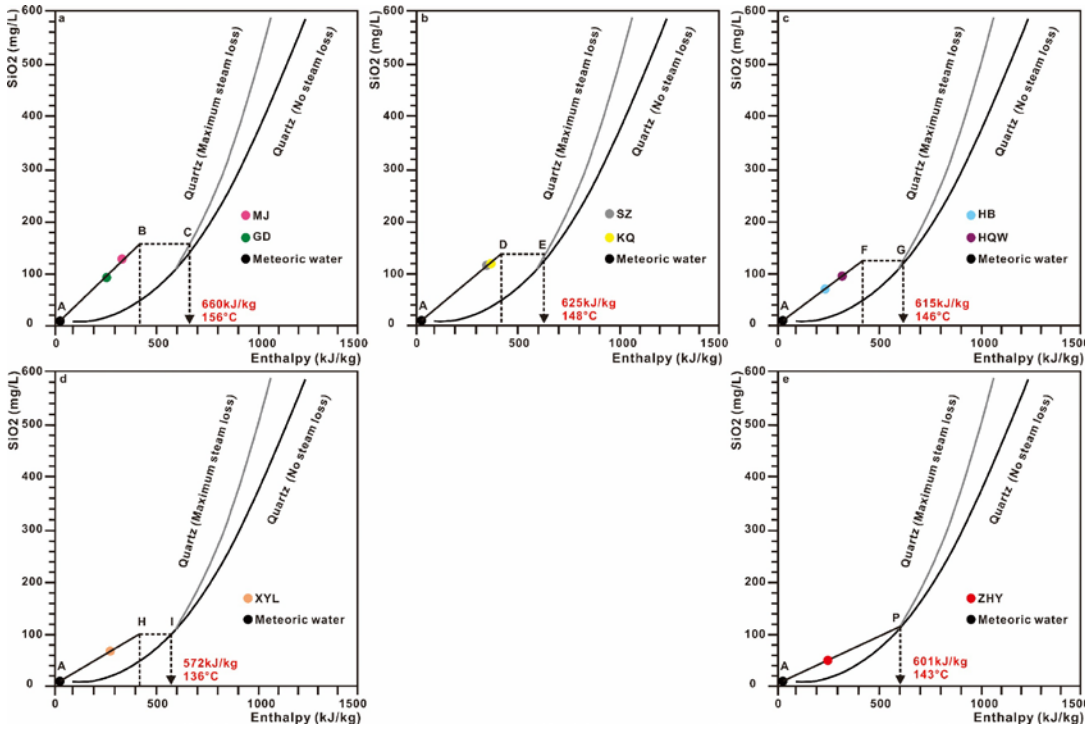

Fig. 16 Silica–enthalpy model for the coastal thermal waters MJ and GD (a), SZ and KQ (b), HB and HQW (c), XYL (d), and ZHY (e).

In summary, the calculated reservoir temperatures by different geothermometers

for the inland and coastal thermal waters cover a relatively limited range of values (Fig. 17). Reservoir temperatures estimated by chalcedony geothermometer are in the range of 62-148 °C and 68-128°C with respect to inland and coastal waters respectively. Multi-mineral saturation states show reservoir temperatures of 90-162 °C for inland thermal waters and 108-134°C for coastal thermal waters. Temperature estimations by anhydrite/chalcedony range between 105 °C and 154 °C for inland hot waters and between 104 °C and 131°C for coastal hot waters. The ranges of 137-167 °C and 136-156°C by silica-enthalpy mixing model correspond to inland and geothermal waters respectively. It is observed that these calculated geothermometers provide reasonable results which best fit values ranging from 90 to 154 °C and 104 to 156 °C with respect to inland and coastal waters respectively, and thus the ranges can be identified as the most reliable reservoir temperatures.

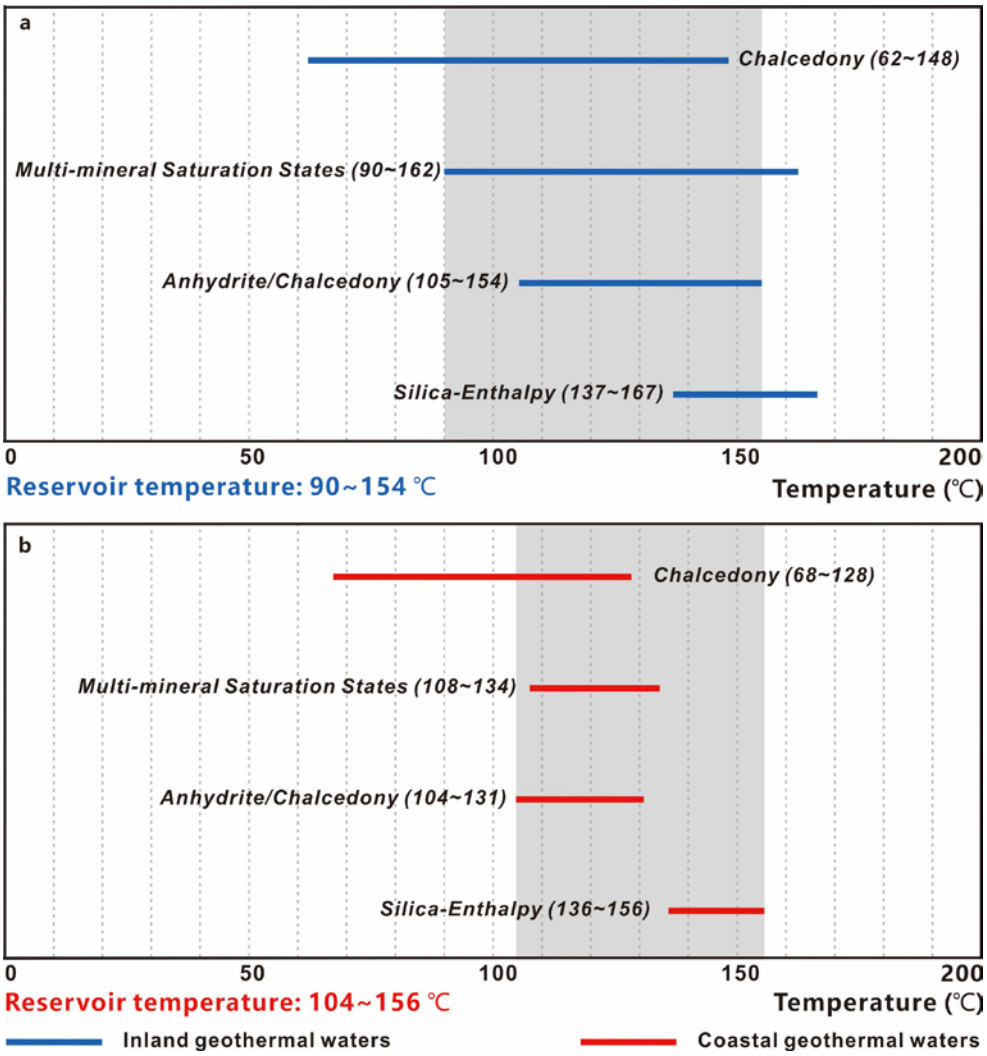

Fig. 17 Comparison of calculated geothermometers from inland (a) and coastal geothermal waters (b) in the PRD region

To quantify the mixing processes, the mixing ratios of near surface cold water in the inland samples on the basis of this model can be assessed in this equation: $X_c = (H_s - H_i) / (H - H_i) \times 100$ (Guo et al., 2017). X_c is the ratios of cold water mixing, H_s is the enthalpy of thermal water sample, and H_i, H represent the enthalpies of initial thermal fluids and cold water, respectively. The results reveal that inland thermal waters have high cold water contributions, varying from 52% (HL and HR) to 78% (ZX) (Table 5). The contribution of seawater in the coastal waters can be estimated using Cl^- as a conservative tracer (Wang and Jiao, 2012), as shown in the following mixing equation: $X_s = (C - C_c) / (C_s - C_c) \times 100$. X_s is the contribution of seawater, C is the Cl^- concentration of coastal water, and C_s, C_c represent the Cl^- concentration of seawater and cold freshwater, respectively (C_s = 18132.7 mg/L, C_c = 6.2 mg/L). This evaluation shows a wide range of seawater contributions to the coastal waters, from 1% (sample KQ, GD) to 37% (sample MJ) (Table 5).

Table 5 Seawater and cold water contributions to the geothermal waters of the PRD region

Sample ID	Cold Water (%)	Category	Sample ID	Seawater (%)	Category
HR	52	inland	KQ	1	coastal
HL	52	inland	XYL	2	coastal
JK	77	inland	GD	1	coastal
ZX	78	inland	HB	4	coastal
YFX	70	inland	SZ	27	coastal
TQ	75	inland	MJ	37	coastal
SYL	71	inland	HQW	22	coastal
TS	53	inland	ZHY	18	coastal
JS	65	inland			

Varying proportions of seawater or cold water mixing indicates a remarkable decrease on enthalpies (temperatures) and dissolved silica concentrations. For instance, inland water ZX shows maximum temperature (167 °C) and SiO_2 content (195 mg/L) in deep reservoir (Fig 15b), but 78% of cold groundwater mixing causes a sharp decline in temperature (58 °C) and SiO_2 contents (106 mg/L) at discharge point. Combined with the analysis of mineral saturation state, reservoir temperatures of the PRD geothermal waters are mainly obscured by the degassing of CO_2 and cold water/seawater mixing. But even so, the hydrogeochemistry and geothermometry likely indicate low-mid temperature geothermal resources in the PRD region.

5. Conclusions

The geothermal waters from the PRD region display a wide compositional variability and significant differences in hydrochemical characteristics. The inland geothermal waters are mainly of bicarbonate-dominated type and sulfate-dominated type, while the coastal thermal waters are mainly of chloride-dominated type. High fluoride contents in the thermal waters imply strong water–rock interactions and common ion effect in this region. Linear correlations between chloride and other major components indicate seawater mixing with coastal thermal waters.

The hydrochemical and stable isotopic investigations suggest that the coastal waters are recharged by local precipitation and seawater and that inland thermal waters are derived from the recharge of local precipitation. The activities of tritium reveal that the both inland and coastal thermal waters have modern precipitation components and verify the presence of mixing between older and modern precipitation and seawater involvement. The contributions of cold groundwater in the inland thermal waters can reach up to 78% and the seawater contributions to coastal geothermal waters reach up to 37%. Na–K–Mg ternary diagram reflects that inland and coastal waters are far away from full equilibria line, which indicates that cation geothermometers are not reliable and applicable for the estimation of the reservoir temperatures. Carbonate minerals are oversaturated with thermal waters at discharge temperatures, and sulphate minerals are undersaturated. Chalcedony mineral is considered to be close to equilibrium.

The chalcedony geothermometer gives more appropriate reservoir temperatures in comparison to quartz geothermometers. The mineral saturation states of the thermal waters clearly show the effect of CO_2 degassing. The combination of chalcedony geothermometer, multi-mineral saturation state, anhydrite/chalcedony, and silica-enthalpy mixing model provide the most reliable reservoir temperatures in the range of 90-154 °C and 104-156°C with respect to inland and coastal geothermal waters respectively. CO_2 degassing and cold water/seawater mixing are identified as crucial factors in governing reservoir temperatures in the PRD region. The hydrogeochemistry and geothermometry of geothermal waters likely indicate low-mid temperature geothermal systems in the PRD region.

Acknowledgements

This study was financially supported by the National Key Research and Development Plan of China (grant 2017YFC0601405, 2019YFC0604900) and the

China Geological Survey (DD20190287). The authors would like to thank Zhang Min for providing the sampling sites and Wu Mingliang, Ye Hanqing, Xu Junmin, and Qiu Huibiao for helping collect samples during the field campaign. Two anonymous reviewers, Dr. Christopher Bromley, and Dr. Halldor Armannsson are acknowledged for their constructive comments and suggestions that helped to improve the quality and the clarity of this manuscript.

References

Afsin, M., Allen, D.M., Kirste, D., Durukan, U.G., Gurel, A., Oruc, O., 2014. Mixing processes in hydrothermal spring systems and implications for interpreting geochemical data: a case study in the Cappadocia region of Turkey. Hydrogeology Journal 22(1), 7-23.

Alçiçek, H., Bülbül, A., Alçiçek, M.C., 2016. Hydrogeochemistry of the thermal waters from the Yenice Geothermal Field (Denizli Basin, Southwestern Anatolia, Turkey). Journal of Volcanology and Geothermal Research 309, 118-138.

Alçiçek, H., Bülbül, A., Brogi, A., Liotta, D., Ruggieri, G., Capezzuoli, E., Meccheri, M., Yavuzer, İ., Alçiçek, M.C., 2018. Origin, evolution and geothermometry of the thermal waters in the Gölemezli Geothermal Field, Denizli Basin (SW Anatolia, Turkey). Journal of Volcanology and Geothermal Research 349, 1-30.

Alçiçek, H., Bülbül, A., Yavuzer, İ., Alçiçek, M.C., 2019a. Hydrogeochemical and isotopic assessment and geothermometry applications in relation to the Karahayıt Geothermal Field (Denizli Basin, SW Anatolia, Turkey). Hydrogeology Journal 27(5), 1791-1816.

Alçiçek, H., Bülbül, A., Yavuzer, İ., Cihat Alçiçek, M., 2019b. Origin and evolution of the thermal waters from the Pamukkale Geothermal Field (Denizli Basin, SW Anatolia, Turkey): Insights from hydrogeochemistry and geothermometry. Journal of Volcanology and Geothermal Research 372, 48-70.

Arnorsson, S., 1983. Chemical equilibria in Icelandic geothermal systems—implications for chemical geothermometry investgations. Geothermics 12(2), 199-128.

Avsar, O., Kurtulus, B., Gursu, S., Kuscu, G.G., Kacaroglu, F., 2016. Geochemical and isotopic characteristics of structurally controlled geothermal and mineral waters of Mugla (SW Turkey). Geothermics 64, 466-481.

Baba, A., Saroglu, F., Akkus, I., Ozel, N., Yesilnacar, M.I., Nalbantcilar, M.T., Demir, M.M., Gokcen, G., Arslan, S., Dursun, N., Uzelli, T., Yazdani, H., 2019. Geological and hydrogeochemical properties of geothermal systems in the southeastern region of Turkey. Geothermics 78, 255-271.

Bayram, A.F., Şimşek, Ş., 2005. Hydrogeochemical and Isotopic Survey of Kütahya-Simav Geothermal Field. Proceedings World Geothermal Congress 1-11.

Belhai, M., Fujimitsu, Y., Bouchareb-Haouchine, F.Z., Iwanaga, T., Noto, M., Nishijima, J., 2016. Hydrogeochemical and isotope geochemical study of northwestern Algerian thermal waters. Arab J Geosci 9(3), 1-17.

Bouchaou, L., Michelot, J.L., Qurtobi, M., Zine, N., Gaye, C.B., Aggarwal, P.K., Marah, H., Zerouali, A., Taleb, H., Vengosh, A., 2009. Origin and residence time of groundwater in the Tadla basin (Morocco)

using multiple isotopic and geochemical tools. Journal of Hydrology 379(3-4), 323-338.
Bozdağ, A., 2016. Hydrogeochemical and isotopic characteristics of Kavak (Seydişehir-Konya) geothermal field, Turkey. Journal of African Earth Sciences 121, 72-83.
Chae, G.T., Yun, S.T., Mayer, B., Kim, K.H., Kim, S.Y., Kwon, J.S., Kim, K., Koh, Y.K., 2007. Fluorine geochemistry in bedrock groundwater of South Korea. Sci Total Environ 385(1-3), 272-283.
Chen, L., Ma, T., Du, Y., Xiao, C., Chen, X., Liu, C., Wang, Y., 2016. Hydrochemical and isotopic (2H, 18O and 37Cl) constraints on evolution of geothermal water in coastal plain of Southwestern Guangdong Province, China. Journal of Volcanology and Geothermal Research 318, 45-54.
Chenaker, H., Houha, B., Vincent, V., 2018. Hydrogeochemistry and geothermometry of thermal water from north-eastern Algeria. Geothermics 75, 137-145.
Clark, I., Fritz, P., 1997. Environmental isotopes in hydrogeology. Lewis Publishers, New York, 16-17.
D'Amore, F., Fancelli, R., Caboi, R., 1987. Observations of the application of chemical geothermometers to some hydrothermal systems in Sardinia. Geothermics 16(3), 271-282.
Davraz, A., 2008. Hydrogeochemical and hydrogeological investigations of thermal waters in the Usak Area (Turkey). Environmental Geology 54(3), 615-628.
Delalande, M., Bergonzini, L., Gherardi, F., Guidi, M., Andre, L., Abdallah, I., Williamson, D., 2011. Fluid geochemistry of natural manifestations from the Southern Poroto-Rungwe hydrothermal system (Tanzania): Preliminary conceptual model. Journal of Volcanology and Geothermal Research 199(1-2), 127-141.
Fantong, W.Y., Satake, H., Ayonghe, S.N., Suh, E.C., Adelana, S.M., Fantong, E.B., Banseka, H.S., Gwanfogbe, C.D., Woincham, L.N., Uehara, Y., Zhang, J., 2010. Geochemical provenance and spatial distribution of fluoride in groundwater of Mayo Tsanaga River Basin, Far North Region, Cameroon: implications for incidence of fluorosis and optimal consumption dose. Environ Geochem Health 32(2), 147-163.
Fara, M., Chandrasekharam, D., Minissale, A., 1999. Hydrogeochemistry of Damt thermal springs\ Yemen Republic. Geothermics 28, 241-252.
Fatta, D., Papadopoulos, A., Loizidou, M., 1999. A study on the landfill leachate and its impact on the groundwater quality of the greater area. Environmental Geochemistry and Health 21, 175-190.
Fouillac, C., Michard, G., 1981. Sodium/lithium ratio in water applied to geothermometry of geothermal reservoirs. Geothermics 10(1), 55-70.
Fournier, Truesdell, 1973a. An empirical Na-K-Ca geothepmometer for the natural waters. Geochimica et Cosmochimica Acta 37, 1255-1276.
Fournier, Truesdell, 1973b. An empirical Na–K–Ca geothermometer for natural waters. Geochimica et Coemochimica Acta 37, 1255–1275.
Fournier, R.O., 1977. Chemical geothermometers and mixing models for geothermal systems. Geothermics 5, 41-50.
Fournier, R.O., Potter, R.W., 1982. An equation correlating the solubility of quartz in water from 25 to 900 °C at pressures up to 10,000 bars. Geochimica et Coemochimica Acta 46(10), 1969-1973.
GBGMI, 1988. Local chronicles of the regional geology in Guangdong Province.
Gemici, U., Filiz, S., 2001. Hydrochemistry of the Cesme geothermal area in western Turkey. Journal of

Volcanology and Geothermal Research 110(1-2), 171-187.
Giggenbach, W.F., 1988. Geothermal solute equilibria. Derivation of Na-K-Mg-Ca geoindicators. Geochimica et Cosmochimica Acta 52, 2749-2756.
Giggenbach, W.F., Gonfiantini, R., Jangi, B.L., Truesdell, A.H., 1983. Isotopic and chemical composition of parbati valley geothermal discharges, North-West Himalaya, India. Geothermics 12, 199–222.
Grasby, S.E., Hutcheon, I., 2001. Controls on the distribution of thermal springs in the southern Canadian Cordillera. Canadian Journal of Earth Sciences 38(3), 427-440.
Gueroui, Y., Maoui, A., Touati, H., Guettaf, M., Bousbia, A., 2018. Hydrogeochemical and environmental isotopes study of the northeastern Algerian thermal waters. Environmental Earth Sciences 77(22), 1-14.
Guo, Q., 2012. Hydrogeochemistry of high-temperature geothermal systems in China: A review. Applied Geochemistry 27(10), 1887-1898.
Guo, Q., Pang, Z., Wang, Y., Tian, J., 2017. Fluid geochemistry and geothermometry applications of the Kangding high-temperature geothermal system in eastern Himalayas. Applied Geochemistry 81, 63-75.
Handa, B.K., 1975. Geochemistry and Genesis of Fluoride-Containing Ground Waters in India. groundwater 13(3), 275-281.
Henley, R.W., Truesdell, A.H., Jr., P.B.B., Whitney, J.A., 1985. Fluid-mineral equilibria in hydrothermal systems. Geothermics 14(1), 107-108.
Hernandez, M.P., Wurl, J., 2017. Hydrogeochemical characterization of the thermal springs in northeastern of Los Cabos Block, Baja California Sur, Mexico. Environ Sci Pollut Res Int 24(15), 13184-13202.
Huang, S.P., Liu, J.Q., 2010. Geothermal energy stuck between a rock and a hot place. Nature 463(7279), 293-293.
Huang, Y., Chu, M., 1995. On the ralations between the features of geological formation and the geomorphic growth in Gusngdong province. Yunnan Geographic Environment Research 7(2), 85-89. (in Chinese with English Abstract).
IAEA/WMO, 2010. Global network of isotopes in precipitation. The GNIP Database.
Judit, D.T., Anita, E., József, K., 2015. The chemical characterization of the thermal waters in Budapest, Hungary by using multivariate exploratory techniques. Environmental Earth Sciences 74(12), 7475-7486.
Keenan, J.H., Keyes, F.G., Hill, P.G., Moore, J.G., 1969. Steam tables. Wiley, New York, 162.
Kerr, R.A., 1982. Extracting geothermal energy can be hard. Science 218(4573), 668-669.
Kerr, R.A., 1991. The back burner of geothermal energy. Science 253(5016), 135-135.
Kharaka, Y.K., Mariner, R.H., 1989. Chemical Geothermometers and Their Application to Formation Waters from Sedimentary Basins. Thermal History of Sedimentary Basins Springer-Verlag New York, 99-117.
Lancia, M., Su, H., Tian, Y., Xu, J.T., Andrews, C., Lerner, D.N., Zheng, C.M., 2020. Hydrogeology of the Pearl River Delta, southern China. J Maps 16(2), 388-395.
Li, J.X., Sagoe, G.D., Yang, G., Lu, G.P., 2018. Evaluation of mineral-aqueous chemical equilibria of felsic reservoirs with low-medium temperature: A comparative study in Yangbajing geothermal field and Guangdong geothermal fields. Journal of Volcanology and Geothermal Research 352, 92-105.

Liao, Z.J., 2012. Promoting the development and utilization of low-medium temperature convection type geothermal resources. commentary 30(32), 80. (Abstract In Chinese).

Lin, B., Yang, S., Zhu, B., Wu, H., 2006. Geological structure and basic geotechnical characteristics in Guangdong province. Chinese Journal of Rock Mechanics and Engineering 25(2), 3337-3346. (in Chinese with English abstract).

Lu, G.P., Wang, X., Li, F.S., Xu, F.Y.M., Wang, Y.X., Qi, S.H., Yuen, D., 2017. Deep geothermal processes acting on faults and solid tides in coastal Xinzhou geothermal field, Guangdong, China. Physics of the Earth and Planetary Interiors 264, 76-88.

Lu, X., Yao, T., Fung, J.C.H., Lin, C., 2016. Estimation of health and economic costs of air pollution over the Pearl River Delta region in China. Sci Total Environ 566-567, 134-143.

Lund, J.W., Boyd, T.L., 2016. Direct utilization of geothermal energy 2015 worldwide review. Geothermics 60, 66-93.

Lund, J.W., Freeston, D.H., 2001. World-wide direct uses of geothermal energy 2000. Geothermics 30(1), 29-68.

Luo, J., Pang, Z., Kong, Y., Wang, Y., 2017. Geothermal potential evaluation and development prioritization based on geochemistry of geothermal waters from Kangding area, western Sichuan, China. Environmental Earth Sciences 76(9), 1-20.

Luo, J., Rohn, J., Bayer, M., Priess, A., Wilkmann, L., Xiang, W., 2015. Heating and cooling performance analysis of a ground source heat pump system in Southern Germany. Geothermics 53, 57-66.

Mao, X., Wang, Y., Zhan, H., Feng, L., 2015. Geochemical and isotopic characteristics of geothermal springs hosted by deep-seated faults in Dongguan Basin, Southern China. Journal of Geochemical Exploration 158, 112-121.

Michard, G., 1990. Behaviour of major elements and some trace elements(Li, Rb, Cs, Sr, Fe, Mn, W, F) in deep hot waters from granitic areas. Chemical Geology 89(2), 117-134.

Minissale, A., Magro, G., Vaselli, O., Verrucchi, C., Perticone, I., 1997. Geochemistry of water and gas discharges from the Mt. Amiata silicic complex and surrounding areas (central Italy). Journal of Volcanology and Geothermal Research 79(3-4), 223-251.

Mock, J.E., 1992. Geothermal energy's future. Science 255(5051), 1490-1490.

Mohammadi, Z., Bagheri, R., Jahanshahi, R., 2010. Hydrogeochemistry and geothermometry of Changal thermal springs, Zagros region, Iran. Geothermics 39(3), 242-249.

Mutlu, H., Gulec, N., 1998. Hydrogeochemical outline of thermal waters and geothermometry applications in Anatolia (Turkey). Journal of Volcanology and Geothermal Research 85, 495-515.

Nicholson, K., 1993. Geothermal Fluids-Chemistry and Exploration Techniques. Springer, Berlin, 52-79.

Nieva, D., Nieva, R., 1987. Developments in geothermal energy in Mexico-part twelve. A Cationic Geothermometer for Prospecting of Geothermal Resources. Heat Recovery Systems 7(3), 243-258.

Noorollahi, Y., Taghipoor, S., Sajadi, B., 2017. Geothermal sea water desalination system (GSWDS) using abandoned oil/gas wells. Geothermics 67, 66-75.

Pandey, S.N., Vishal, V., Chaudhuri, A., 2018. Geothermal reservoir modeling in a coupled thermo-hydro-mechanical-chemical approach: A review. Earth-Science Reviews 185, 1157-1169.

Pang, Z., Reed, M., 1998. Theoretical chemical thermometry on geothermal waters: Problems and

methods. Geochimica et Coemochimica Acta 62(6), 1083-1091.
Panno, S.V., Hackley, K.C., Hwang, H.H., Greenberg, S.E., Krapac, I.G., Landsberger, S., O'Kelly, D.J., 2006. Characterization and identification of na-cl sources in ground water. Ground Water 44(2), 176-187.
Park, S.S., Yun, S.T., Chae, G.T., Hutcheon, I., Koh, Y.K., So, C.S., Choi, H.S., 2006. Temperature evaluation of the Bugok geothermal system, South Korea. Geothermics 35(4), 448-469.
Parkhurst, D.L., Appelo, C.A.J., 1999. User's guide to PHREEQC (Version 2): A computer program for speciation, batch-reaction, one-dimensional transport, and inverse geochemical calculations. U.S. Geological Survey Water-Resources Investigations Report.
Pastorellia, S., Marini, L., Hunziker, J.C., 1999. Water chemistry and isotope composition of the Acquarossa thermal system, Ticino, Switzerland. Geothermics(28), 75-93.
Pasvanoglu, S., Celik, M., 2018. A conceptual model for groundwater flow and geochemical evolution of thermal fluids at the Kizilcahamam geothermal area, Galatian volcanic Province. Geothermics 71, 88-107.
Pei, J., Niu, Z., Wang, L., Song, X.P., Huang, N., Geng, J., Wu, Y.B., Jiang, H.H., 2018. Spatial-temporal dynamics of carbon emissions and carbon sinks in economically developed areas of China: a case study of Guangdong Province. Sci Rep 8(1), 13383.
Piper, M., 1944. A graphic procedure in the geochemical interpretation of water-analyses. Transactions American Geophysical Union 25(6), 914-928.
Pirlo, M.C., 2004. Hydrogeochemistry and geothermometry of thermal groundwaters from the Birdsville Track Ridge, Great Artesian Basin, South Australia. Geothermics 33(6), 743-774.
Portugal, E., Izquierdo, G., Truesdell, A., Alvarez, J., 2005. The geochemistry and isotope hydrology of the Southern Mexicali Valley in the area of the Cerro Prieto, Baja California (Mexico) geothermal field. Journal of Hydrology 313(3-4), 132-148.
Reed, M., Spycher, N., 1984. Calculation of pH and mineral equilibria in hydrothermal waters with application to geothermometry and studies of boiling and dilution. Geochimica et Cosmochimica Acta 48, 1479-1492.
Ren, Z., Ye, X., Wei, M., Liao, G., Sun, C., Liu, T., Qiao, J., Wei, W., 2011. Deep fault distribution interpreted by gravity data in the Pearl River Delta Region. Earthquakc Research in Sichuan 4(141), 29-34. (in Chinese).
Rezaei, A., Rezaeian, M., Porkhial, S., 2019. The hydrogeochemistry and geothermometry of the thermal waters in the Mouil Graben, Sabalan volcano, NW Iran. Geothermics 78, 9-27.
Saxena, V.K., Ahmed, S., 2001. Dissolution of fluoride in groundwater: a water-rock interaction study. Environmental Geology 40(9), 1084-1087.
Sharifi, R., Moore, F., Mohammadi, Z., Keshavarzi, B., 2016. Estimation of deepwater temperature and hydrogeochemistry of springs in the Takab geothermal field, West Azerbaijan, Iran. Environmental Monitoring and Assessment 188(1), 1-20.
Stefansson, V., 2000. The renewability of geothermal energy. Proceedings World Geothermal Congress, 883-888.
Tarcan, G., Gemici, U., 2003. Water geochemistry of the Seferihisar geothermal area, Izmir, Turkey. Journal of Volcanology and Geothermal Research 126(3-4), 225-242.

Tian, J., Pang, Z.H., Guo, Q., Wang, Y.C., Huang, T.M., Kong, Y.L., 2018. Geochemistry of geothermal fluids with implications on the sources of water and heat recharge to the Rekeng high-temperature geothermal system in the Eastern Himalayan Syntax. Geothermics 74, 92-105.

Truesdell, A.H., Hulston, J.R., 1980. Isotopic evidence on environments of geothermal systems. Handbook of environmental isotope geochemistry, 179-226.

Turali, E.Y., Simsek, S., 2017. Conceptual and 3D simulation modeling of the Sorgun hydrothermal reservoir (Yozgat,Turkey). Geothermics 66, 85-100.

Verma, S.P., Pandarinath, K., Santoyo, E., Gonzalez-Partida, E., Torres-Alvarado, I.S., Tello-Hinojosa, E., 2006. Fluid chemistry and temperatures prior to exploitation at the Las Tres Virgenes geothermal field, Mexico. Geothermics 35(2), 156-180.

Wang, J., Jin, M., Jia, B., Kang, F., 2015. Hydrochemical characteristics and geothermometry applications of thermal groundwater in northern Jinan, Shandong, China. Geothermics 57, 185-195.

Wang, X., Lu, G.P., Hu, B.X., 2018. Hydrogeochemical Characteristics and Geothermometry Applications of Thermal Waters in Coastal Xinzhou and Shenzao Geothermal Fields, Guangdong, China. Geofluids, 1-23.

Wang, Y., Jiao, J.J., 2012. Origin of groundwater salinity and hydrogeochemical processes in the confined Quaternary aquifer of the Pearl River Delta, China. Journal of Hydrology 438-439, 112-124.

Warner, N.R., Kresse, T.M., Hays, P.D., Down, A., Karr, J.D., Jackson, R.B., Vengosh, A., 2013. Geochemical and isotopic variations in shallow groundwater in areas of the Fayetteville Shale development, north-central Arkansas. Applied Geochemistry 35, 207-220.

Waterloo, 2014. Demonstration Guide for AquaChem 2014.2. waterloohydrogeologic.

WHO, 2004. Guidelines for drinking-water quality, 3rd edition: Volume 1, Chapter. World Health Organization Geneva, Switzerland.

Xi, Y.F., Wang, G.L., Liu, S., Zhao, Y.B., Hu, X.Y., 2018. The formation of a geothermal anomaly and extensional structures in Guangdong, China: Evidence from gravity analyses. Geothermics 72, 225-231.

Yang, P., Cheng, Q., Xie, S., Wang, J., Chang, L., Yu, Q., Zhan, Z., Chen, F., 2017. Hydrogeochemistry and geothermometry of deep thermal water in the carbonate formation in the main urban area of Chongqing, China. Journal of Hydrology 549, 50-61.

Yang, P., Dan, L., Groves, C., Xie, S., 2019a. Geochemistry and genesis of geothermal well water from a carbonate–evaporite aquifer in Chongqing, SW China. Environmental Earth Sciences 78(1), 1-14.

Yang, P., Luo, D., Hong, A., Ham, B., Xie, S., Ming, X., Wang, Z., Pang, Z., 2019b. Hydrogeochemistry and geothermometry of the carbonate-evaporite aquifers controlled by deep-seated faults using major ions and environmental isotopes. Journal of Hydrology 579, 124116.

Yin, L.J., Luo, Y.Z., Ma, H.Y., Xie, Y.X., Liu, Z.Z., 2017. Development situation and prospecting division of geothermal resources in Yangshan county, Guangdong Province.

Yurteri, C., Simsek, S., 2017. Hydrogeological and hydrochemical studies of the Kaman-Savcili-Büyükoba (Kirsehir) geothermal area, Turkey. Geothermics 65, 99-112.

Zainal, S., Ismail, M.A.M., Mostafa, R., Narita, N., Mahmood, N., Ng, S.M., 2016. Hydrogeochemistry of tunnel seepage water along the contact of zone of metasedimentary and granitic rock within the Pahang-Selangor Raw Water Transfer Tunnel Project, Malaysia. Arab J Geosci 9(4), 1-11.

Zhang, X., 2009. Hydrogeological Condition of Guangdong Province. Guangdong Highway Survey and Design 3(135), 28-30. (in Chinese).

Zhao, X.G., Wan, G., 2014. Current situation and prospect of China's geothermal resources. Renew Sust Energ Rev 32, 651-661.

Zhou, X.M., Li, W.X., 2000. Origin of Late Mesozoic igneous rocks in Southeastern China: implications for lithosphere subduction and underplating of mafic magmas. Tectonophysics 326, 268-287.

Zhu, W., Hong, Z., Li, X., He, D., Song, X., Tao, R., Chen, Z., Sun, H., Liao, J., 2010. The early Jurassic mafic–ultramafic intrusion and A-type granite from northeastern Guangdong, SE China: Age, origin, and tectonic significance. Lithos 119(3-4), 313-329.

Zong, Y., Yim, W.W.S., Yu, F., Huang, G., 2009. Late Quaternary environmental changes in the Pearl River mouth region, China. Quaternary International 206(1-2), 35-45.